



# Effect of Na content and thermal treatment of titanate nanotubes on the photocatalytic degradation of formic acid



Asma Turki<sup>a,b</sup>, Hafedh Kochkar<sup>a,c,\*\*</sup>, Chantal Guillard<sup>d</sup>, Gilles Berhault<sup>d,\*</sup>, Abdelhamid Ghorbel<sup>a</sup>

<sup>a</sup> Laboratoire de Chimie des Matériaux et Catalyse, Faculté des Sciences de Tunis, 2092 El Manar, Tunis, Tunisia

<sup>b</sup> Laboratoire des Matériaux Utiles, Institut National de Recherche et d'Analyse Physico-chimique, Pôle Technologique de Sidi Thabet 2020, Tunisia

<sup>c</sup> Centre National de Recherches en Sciences des Matériaux (CNRSM), Technopôle Borj-Cédria, 8027 Soliman, Tunisia

<sup>d</sup> Institut de Recherches sur la Catalyse et l'Environnement, IRCELYON, CNRS – University of Lyon, Villeurbanne, 69100, France

## ARTICLE INFO

### Article history:

Received 14 November 2012

Received in revised form 18 February 2013

Accepted 5 March 2013

Available online 18 March 2013

### Keywords:

Titanates

Nanotubes

Sodium

Thermal stability

Photocatalytic activity

## ABSTRACT

The influence of the sodium content on thermal stability and photocatalytic activity of calcined titanate nanotubes (TNT) was herein evaluated by preparing different samples through hydrothermal treatment of TiO<sub>2</sub> powder (P25) in a concentrated NaOH solution (11.25 M) at 130 °C during 20 h followed by acid washing steps. Titanate nanotubes samples with sodium (Na-TNT) and sodium-free (H-TNT) were then obtained using different concentrations of HCl aqueous solutions namely 0.1 M and 1 M respectively. As synthesized nanomaterials with different Na percentages were then calcined at temperatures varying between 400 °C and 700 °C. Samples were characterized by means of nitrogen adsorption-desorption isotherms at 77 K, thermal analysis (DTA, TGA), transmission electron microscopy (TEM), X-ray diffraction (XRD), Raman spectroscopy, and diffuse reflectance spectroscopy (DRS). The photocatalytic activities of Na-TNT and H-TNT derived nanomaterials were then evaluated through the photocatalytic degradation of formic acid (FA).

Results show that the presence of sodium retards the dehydration process during the transformation of titanate into TiO<sub>2</sub> shifting the formation of anatase phase to higher temperatures. However, sodium is not necessary to preserve the nanotubular morphology. The presence of sodium after calcination strongly impacts negatively the photocatalytic properties. If sodium is completely removed from the initial titanate orthorhombic phase, calcination leads to TiO<sub>2</sub> anatase materials with enhanced photocatalytic properties compared to P25 in the degradation of formic acid, particularly if nanotubular morphology is preserved. The highest activity was therefore achieved for the H-TNT sample calcined at 400 °C. The photodegradation activity of formic acid depends on the specific surface areas and TiO<sub>2</sub> crystallinity. In pure anatase nanoparticles the activity strongly decreases with coherent crystallographic domains  $\geq 10$  nm.

© 2013 Elsevier B.V. All rights reserved.

## 1. Introduction

One-dimensional TiO<sub>2</sub> related nanomaterials with high morphological specificity, such as nanotubes, nanowires, nanofibers and nanorods, have attracted considerable attention due to their interesting chemical and physicochemical properties [1]. These nanostructured TiO<sub>2</sub> materials have interesting potential applications in various fields such as medicine [2–4], electrochemistry

[5–7], environment purification [8–10], gas sensors [11,12], heterogeneous catalysis [13–16] and photocatalysis [17–19].

The elaboration of 1D TiO<sub>2</sub> related materials with different morphologies and high purity may occur using three general approaches: (i) the chemical “template” method [20–22], (ii) the electrochemical “anodic oxidation” method [23,24], and (iii) the alkaline hydrothermal treatment [25,26]. For large scale production of nanostructured TiO<sub>2</sub> materials, the hydrothermal method, proposed by Kasuga et al. [25,27], is the most suitable. It involves treating the precursor of TiO<sub>2</sub> (anatase and/or rutile) in an autoclave by a concentrated alkaline solution (NaOH and/or KOH) at high temperature for a relatively long time followed by a washing step with water and acid solutions. This method is simple and not expensive. With respect to the described methods, the alkaline hydrothermal route remains the most versatile for the production of 1D titanate nanotubes with tunable diameters (~8–200 nm) [28]. Several factors can influence the formation of titania nanotubes such as: the

\* Corresponding author. Tel.: +33 472 44 53 24; fax: +33 472 44 53 99.

\*\* Corresponding author at: Laboratoire de Chimie des Matériaux et Catalyse, Faculté des Sciences de Tunis, 2092 El Manar, Tunis, Tunisia. Tel.: +216 22 96 04 26; fax: +216 79 32 53 14.

E-mail addresses: [soumaturk@yahoo.fr](mailto:soumaturk@yahoo.fr) (A. Turki), [h.kochkar@yahoo.fr](mailto:h.kochkar@yahoo.fr) (H. Kochkar), [Gilles.Berhault@ircelyon.univ-lyon1.fr](mailto:Gilles.Berhault@ircelyon.univ-lyon1.fr) (G. Berhault).

structure of the starting material (anatase, rutile or amorphous), the nature and concentration of the alkaline solution, the hydrothermal temperature and duration and the post-treatment processes (acid washing and calcination) [28–33].

The assignment of the structure of titanate nanotubular materials was the subject of intense controversy. In its initial study, Kasuga et al. [25] characterized their product as anatase. This assumption was confirmed in a more recent paper [34]. On the contrary, on the basis of XRD, selected-area electron diffraction (SAED) and high-resolution transmission electron microscopy (HRTEM) data, Peng et al. [14,35] proposed that the crystal structure of titanate nanotubes corresponds to the layered trititanic acid ( $\text{H}_2\text{Ti}_3\text{O}_7$ ) with a monoclinic crystal structure. On the basis of XRD and transmission electron microscopy (TEM) data, Nakahira et al. [36] assigned HNTs produced using alkaline hydrothermal treatment to a tetratitanic acid,  $\text{H}_2\text{Ti}_4\text{O}_4(\text{HO})_2$ . On the basis of studies of the sodium content of titanate nanotubes at various pH values, during acid washing (in combination with XRD and TEM data), Yang et al. [37] proposed the following crystal structure of titanate nanotubes:  $\text{H}_2\text{Ti}_2\text{O}_5 \cdot \text{H}_2\text{O}$  with an orthorhombic unit cell. In conclusion, nanotubes are assumed to be layered protonated polytitanates ( $\text{H}_{2-x}\text{M}_x\text{Ti}_n\text{O}_{2n+1}$  with  $\text{M} = \text{Na}$  or  $\text{K}$ ;  $x \leq 2$ ;  $n = 2, 3, 4$  or  $5$ ) and sodium can be exchanged under acidic medium.

The nanotubular architectures of these new photocatalytic materials trigger the interest to exploit them in the wastewater treatment field. In this respect, the photocatalytic activity of titanate nanotubes strongly depends on the nature of the pollutant [38], the crystallographic structure [39], the calcination treatment [40–42], and the presence of alkali ions ( $\text{Na}^+$ ,  $\text{K}^+$ ) in the structure. One of the important factors responsible for the different photocatalytic activities of nanotubes may be related to the amount of sodium content present in the samples. Sodium ions also play a crucial role in the morphological and structural stability as a function of the calcination temperature [43].

However, in the literature, there are considerable uncertainties about the photocatalytic properties of titanate nanotubes. In this respect, the photodegradation of acetone in air was successfully found to occur by Yu et al. using calcined samples of nanowires at  $500^\circ\text{C}$  [44], these samples showing a photocatalytic activity 1.8 times higher than Degussa P25. Samples initially obtained by hydrothermal treatment with KOH were washed with 0.1 M HCl aqueous solution and the higher photocatalytic activity was ascribed to the combination of high surface area, high pore volume, and the presence of the  $\text{TiO}_2$  brookite phase. According to Jitputti et al. [45], calcined samples of nanowires showed higher photocatalytic activity with respect to P25 (particularly after post-treatment at  $500^\circ\text{C}$ ) for the photocatalytic  $\text{H}_2$  evolution from water splitting reaction using methanol as sacrificial reagent. Contrary to Yu et al., the highest photocatalytic activity was found to occur on  $\text{TiO}_2$  anatase nanowires while hydrogen titanate was found almost inactive. Alkali-containing titanates were not evaluated in both cases. Moreover, Mozia et al. found that nanotubular hydrogen titanate (synthesized at  $140^\circ\text{C}$ , 48 h) did not exhibit photocatalytic activity for the degradation of a model azo dye (Acid Red 18) [46]. However, these materials were successfully applied for the photocatalytic generation of  $\text{CH}_4$  and  $\text{H}_2$  in a solution of acetic acid. However, the presence or absence of sodium in these samples was not clearly demonstrated.

In contrast, Qamar et al. [43] first observed that titanate nanotubes (whatever the amount of sodium present) showed no photocatalytic activity for the degradation of the amaranth dye. After calcination at  $400^\circ\text{C}$  (for sodium-free sample) or  $500^\circ\text{C}$  (if sodium is only partially replaced by hydrogen), the photocatalytic activity reached its maximum but these samples remained less active than P25. However, the role of sodium was not precisely evaluated since not quantified while the relationship between

photocatalytic activity and morphology was not clearly defined. Zhang et al. [47] observed that the highest activity in the photooxidation of propylene was obtained on hydrogen titanate nanotubes calcined at  $500^\circ\text{C}$  while the breakdown of the nanotube morphology occurring simultaneously with the formation of anatase leads to a loss in photocatalytic activity. On the opposite, sodium titanate nanotubes were found inactive. Lee et al. [48] evaluated titanate nanotubes presenting different amounts of sodium in the photocatalytic oxidation of a basic dye, e.g. basic violet 10 (BV 10). Again, no clear relationship with the sodium content was observed since the highest photocatalytic activity (lower than P25) was observed for the sample presenting a medium content of sodium. Finally, a recent study by Bem et al. [49] tried to establish the influence of the replacement of sodium by protons for the degradation of rhodamine 6G. The complete removal of sodium did not lead to a higher photocatalytic decolorization than in the presence of Na even if the protonated sample avoided the formation of new secondary aromatic products.

Furthermore, the direct impact of sodium on the photocatalytic properties (independently of the morphology present) or its indirect role through the maintaining of the nanotubular structure which would be necessary for enhancing the photocatalytic activity is not clearly established. In this respect, most of the studies did not determine the residual amount of sodium present in their samples after the acid washing procedure limiting the possibility to evaluate clearly the impact of sodium on structural and photocatalytic properties.

The aim of our work is to elaborate and characterize titanate nanotubes (Na-TNT) or free sodium samples (H-TNT). A systematic study, therefore, will be carried out to determine the effect of calcination as function of the sodium content on the photocatalytic activity of nanotubes, photocatalytic activity affected by the resulting phase, shape and surface area. The photocatalytic reaction used herein will be the degradation of formic acid (FA) in aqueous solution under atmospheric conditions. Formic acid was chosen because of its direct mineralization to  $\text{CO}_2$  (gas) and  $\text{H}_2\text{O}$  (liquid) without formation of any stable intermediates [50–55]. In addition, this reaction represents the final step in the photodegradation of many complex organic compounds.

## 2. Materials and methods

### 2.1. Reagents

The reagents included NaOH, HCl, and  $\text{HCOOH}$  were supplied by Fisher Chemicals and Acros Organics. Titanium dioxide ( $\text{TiO}_2$  (P25), 72% anatase – 28% rutile,  $50\text{ m}^2\text{ g}^{-1}$ ) was provided by Degussa-Hüls-AG. Ultrapure water ( $18\text{ M}\Omega\text{ cm}^{-1}$ ) was used throughout the whole experiments.

### 2.2. Elaboration of titanate nanotubes

Titanate nanotubes were prepared following the same protocol used in our previous work [56,57] via alkaline hydrothermal treatment. 3.0 g of  $\text{TiO}_2$  powder (P25) were treated with 90 mL of  $11.25\text{ mol L}^{-1}$  NaOH aqueous solution in a 150 mL Teflon-lined autoclave at  $130^\circ\text{C}$  for 20 h. The resulting precipitate was recovered by filtration and washed with distilled water and a  $0.1\text{ mol L}^{-1}$  HCl solution until the pH value of the rinsing solution reached ca. 6.5. This sample was dried at  $80^\circ\text{C}$  for 24 h, named Na-TNT, and then calcined at 400, 500, 600 and  $700^\circ\text{C}$  in air for 2 h, respectively. These samples were then named Na-TNT-400, Na-TNT-500, Na-TNT-600 and Na-TNT-700, respectively.

In order to elaborate free sodium materials, a second washing step of Na-TNT was performed using a more concentrated solution

of hydrochloric acid ( $1 \text{ mol L}^{-1}$ ) while ultrapure water was used. The obtained nanomaterials were called H-TNT. These nanomaterials were then calcined at different temperatures in air following the same protocol used for Na-TNT samples and were labeled H-TNT-400, H-TNT-500, H-TNT-600 and H-TNT-700. For comparison purpose, a sodium free titanate sample was also calcined at  $330^\circ\text{C}$  and labeled H-TNT-330.

### 2.3. Characterization

Sodium amounts were evaluated by inductively coupled plasma optical emission spectrometry (ICP-OES) measurements using a Horiba Jobin Yvon Activa apparatus. Prior to analysis, samples undergo attack by a mixture of acids, namely  $\text{H}_2\text{SO}_4$ ,  $\text{HNO}_3$  and  $\text{HF}$ , in a 1:1:0.5, v/v/v ratio before maximum evaporation. The remaining volume is then diluted again in  $\text{HNO}_3$ .

Low temperature nitrogen adsorption measurements were done using a Micromeritics ASAP 2020 instrument. The Brunauer–Emmett–Teller (BET) specific surface areas ( $S_{\text{BET}}$ ) were determined by a multipoint BET method using the adsorption data in the relative pressure  $P/P_0$  range of 0.05–0.25. Desorption isotherms were used to determine the pore size distribution using the Barrett–Joyner–Halenda (BJH) method. The nitrogen adsorption volumes at the relative pressure ( $P/P_0$ ) of 0.95 were used to determine the total pore volumes.

The thermal stability was studied through TGA and DTA measurements using a SETARAM (Setsys Evolution) apparatus equipped with alumina support. A heating rate of  $5^\circ\text{C min}^{-1}$  was used from room temperature to  $700^\circ\text{C}$  under air atmosphere.

The phase identification of the sample was done by X-ray Diffraction (XRD) analyses using a Bruker D8 Advance A25 diffractometer with  $\text{Cu-K}\alpha$  radiation ( $\lambda = 1.54184 \text{ \AA}$ ). The “HighScore Plus” software was used for the identification of phases. The weight percentage estimation of several phases present in some samples was made using the Rietveld method.

Raman spectra were recorded at  $20^\circ\text{C}$  using a LabRAM-HR instrument (Horiba Jobin Yvon) from  $100 \text{ cm}^{-1}$  to  $1000 \text{ cm}^{-1}$  with spectral resolution of  $4.0 \text{ cm}^{-1}$ , a 514 nm argon–krypton RM2018 laser as incident light, and a CCD detector cooled at  $-75^\circ\text{C}$ . The average power at the surface of the studied samples was fixed at 1 mW.

The morphology of the different samples was studied by Transmission Electron Microscopy (TEM) and High Resolution TEM (HRTEM) using a JEOL 2010 instrument operating at 200–400 kV. The microscope was equipped with an ultrahigh-resolution polar piece (point resolution:  $1.9 \text{ \AA}$ ). The specimens for TEM analysis were prepared by dropping and drying the colloidal solution onto a holey carbon film supported on a Cu grid (300 mesh).

Measurement of the band gap energies was performed using UV–vis diffuse reflectance AvaSpec-2048 Fiber Optic Spectrometer equipped with a symmetrical Czerny–Turner design with 2048 pixel CCD detector array. Spectra were recorded from 250 nm to 800 nm. A barium sulfate pellet was used as a blank white reference.

### 2.4. Adsorption experiments

A volume of 30 mL of formic acid with different initial concentrations was stirred under dark conditions during 30 min. This time was necessary to reach the equilibrium between adsorption and desorption (for all materials). A concentration of  $1 \text{ g L}^{-1}$  of each sample was used. The pH of the solutions was ca.  $3.0 \pm 0.5$  depending on the concentration used. Samples were filtered using  $0.45 \text{ }\mu\text{m}$  Millipore filters and analyzed using a VARIAN ProStar High Performance Liquid Chromatograph (HPLC) equipped with a COREGEL-87H3 column ( $300 \text{ mm} \times 7.8 \text{ mm}$ ) and a UV–vis detector

( $\lambda_{\text{max}} = 210 \text{ nm}$ ). A  $\text{H}_2\text{SO}_4$  ( $5 \times 10^{-3} \text{ mol L}^{-1}$ ) mobile phase was used flowing at  $0.7 \text{ mL min}^{-1}$ .

### 2.5. Photocatalytic experiments

The photoreaction was carried out in a Pyrex cylindrical flask ( $100 \text{ cm}^3$ ) using an optical window with a  $12.5 \text{ cm}^2$  area. The radiant flux was provided by a high-pressure mercury lamp Philips HPK 125 W which provides maximum energy at 365 nm. An optical Corning filter 0.52 in conjunction with a circulating water system was installed to cut-off wavelength below 340 nm and to avoid from heating the solution under UV irradiation. The distance between the bottom of the reactor and the UV source is 3 cm. The magnetic stirrer is set at 450 rpm. The radiant flux was measured with a VLX-3W radiometer with a CX-365 detector (UV-A). Sample concentration of  $1 \text{ g L}^{-1}$  was used with a 30 mL volume of FA solution of different initial concentrations. At regular time intervals of FA photodegradation, samples were taken, filtered using  $0.45 \text{ }\mu\text{m}$  Millipore filters, and analyzed with HPLC.

## 3. Results and discussion

### 3.1. Elemental analysis

Since the objective of our study is related to the influence of the sodium content on the morphological and photocatalytic properties of calcined titanate nanotubes, the first point to be considered is the efficacy of the acid washing procedure in order to remove sodium from the samples issued from the alkaline hydrothermal method. The sodium content of the Na-TNT and H-TNT samples obtained after hydrothermal treatment followed by an acid washing treatment respectively at HCl concentrations of 0.1 M and 1.0 M was therefore determined by ICP-OES. The washing treatment at 0.1 M HCl of the Na-TNT sample only leads to a partial replacement of  $\text{Na}^+$  ions by  $\text{H}^+$  ions since a sodium content of 6.0 wt% is still measured by ICP-OES analysis. Considering that the titanate compounds obtained correspond to the following formula  $\text{Na}_x\text{H}_{2-x}\text{Ti}_2\text{O}_5 \cdot \text{H}_2\text{O}$  phase (see below XRD results), the sodium amount present would correspond to a stoichiometry  $\text{Na}_{0.53}\text{H}_{1.47}\text{Ti}_2\text{O}_5 \cdot \text{H}_2\text{O}$  showing that 26% of sodium was not removed following this acid washing procedure. The washing procedure of the H-TNT sample using 1.0 M HCl under vigorous stirring for 30 min leads to the complete removal of sodium from the layered titanate samples since a very low amount of sodium ( $\approx 0.02 \text{ wt\%}$ ) was determined in this case. Our result is in agreement with the study by Poudel et al. [58] showing that to obtain in high yield a pure hydrogenotitanate phase without sodium, the acid concentration used during the washing procedure must be maintained between 0.5 and 1.5 M. Acid concentrations below 0.5 M were found to be ineffective in sodium ions removal in agreement with the present results and those of Morgado et al. [59]. On the opposite, acid concentrations above 2.0 M would damage the nanotubular morphology leading to the formation of clumps of irregular particles of about 100 nm in size.

### 3.2. Transmission electron microscopy

#### 3.2.1. Na-TNT samples before and after calcination

TEM images of the Na-TNT sample before calcination are reported in Fig. 1A and B. The as-formed initial Na-TNT sample already presents hollow nanotubular morphology with an outer diameter of  $\leq 15 \text{ nm}$  and a length of several hundred nanometers. This result should be first considered in the framework of the mechanism proposed to explain the formation of titanate nanotubes. Indeed, even if still controversial, the mechanism of formation of titanate nanotubes is believed to comprise three general steps: (i)

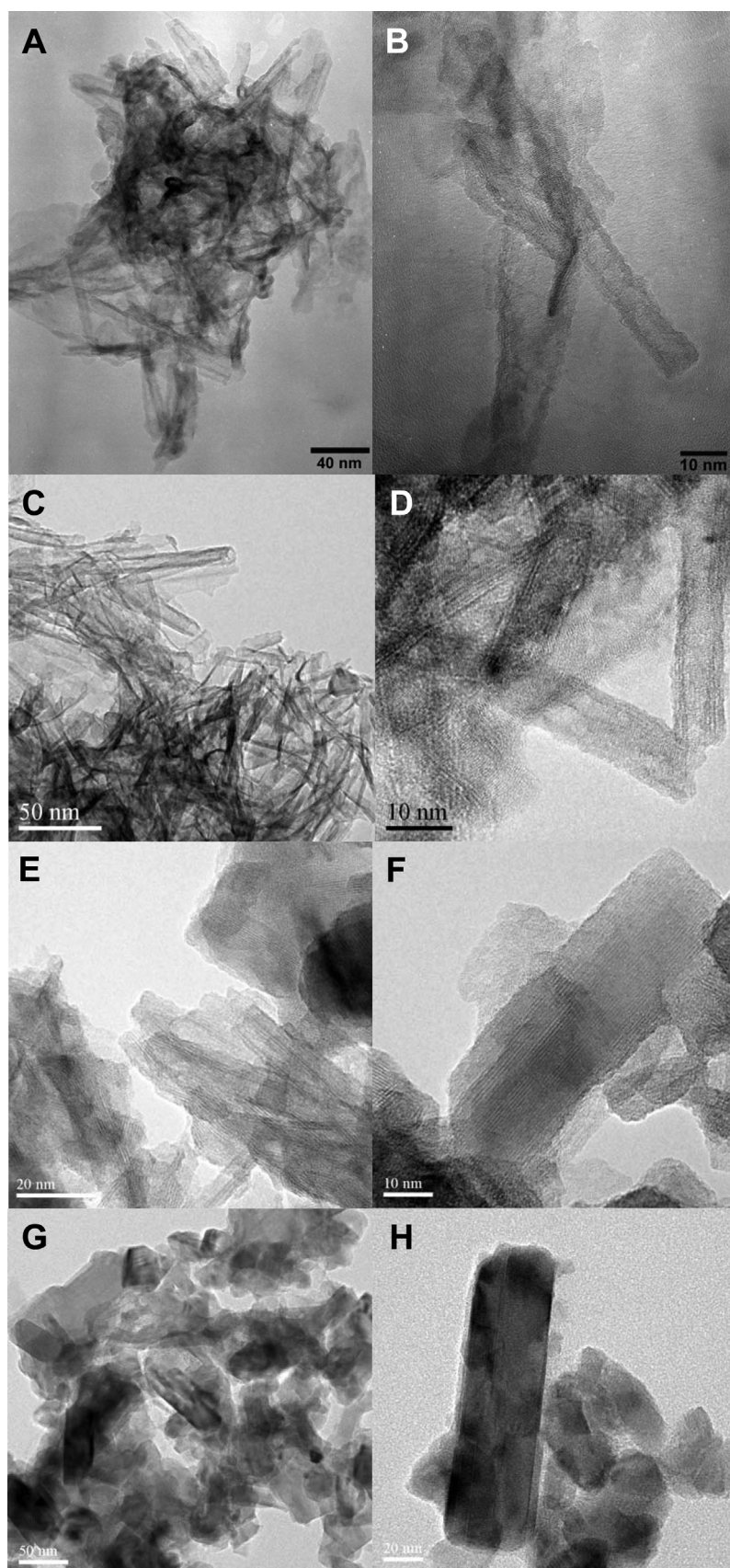


**Fig. 1.** TEM pictures of the Na-TNT samples before calcination (A and B) and after calcination at 400 °C (C and D), 500 °C (E and F), and 600 °C (G and H).



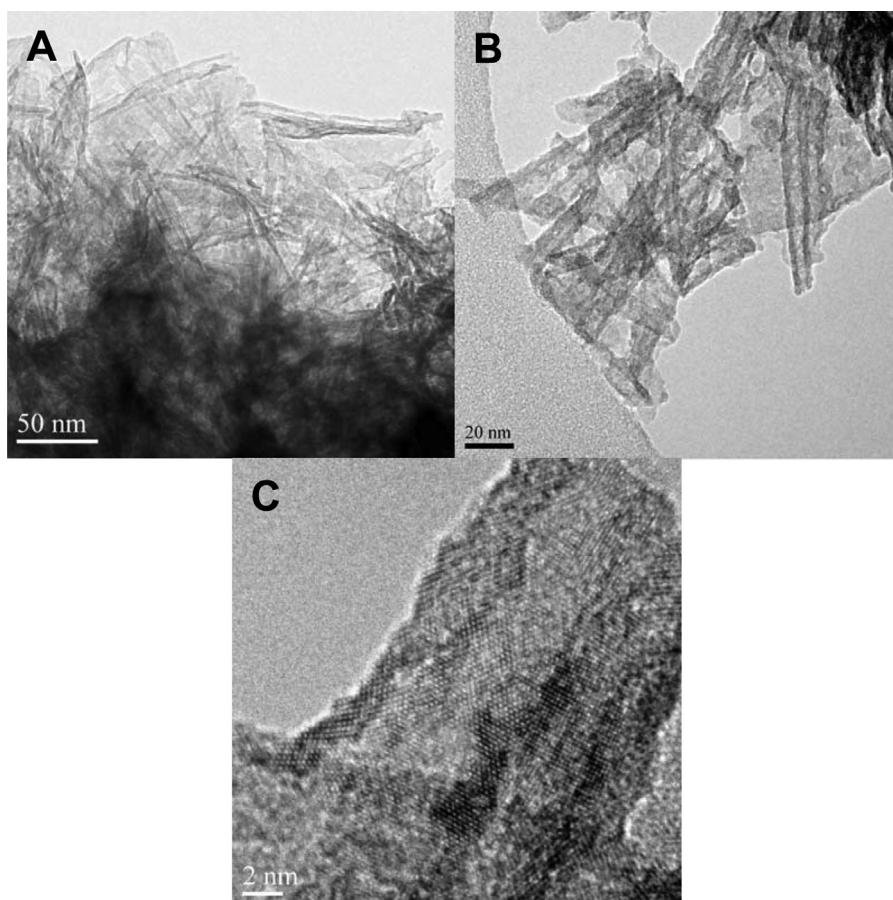


**Fig. 2.** TEM pictures of the as-initially formed H-TNT sample showing its nanotubular morphology (A and B). HRTEM picture (C) of the extremity of one of the titanate nanotube.

dissolution of the  $\text{TiO}_2$  particles under the strong alkaline conditions leading to the breaking of Ti—O—Ti bonds, (ii) simultaneous formation of Na—Ti—O bonds forming lamellar sheets, and (iii) destabilization of the lamellar sheets due to the acid washing procedure removing alkaline ions and leading to the rolling of the nanosheets into nanotubes in order to remove dangling bonds [25,27,60–62]. The formation of titanate nanotubes in the case of the Na-TNT sample therefore suggests, if one assumes this general mechanism, that partial replacement of sodium ions during the washing procedure with 0.1 M HCl solution is sufficient to induce rolling of nanosheets into nanotubes. In the present case, nanotubes exhibit a multilayered aspect resulting from the folding of two to five nanosheets.

After calcination at  $400^\circ\text{C}$ , the Na-TNT-400 sample still maintains its nanotubular morphology (Fig. 1C). The hollow aspect of the nanotubes can be clearly observed. The wall thickness is about 2 nm with an outer diameter of 8–10 nm. Crystallinity appears slightly better than for the as-formed Na-TNT sample. However, fringes are still only partly observed on some nanotubes (Fig. 1D). Calcination at  $400^\circ\text{C}$  therefore hardly modifies the morphology of the titanate samples presenting a high amount of sodium.

On the opposite, calcination at  $500^\circ\text{C}$  leads to a partial loss of the nanotubular morphology of the Na-TNT-500 sample with formation of plate-like particles (Fig. 1E and F). Interestingly, the width of these plate-like particles correspond to the size expected when unfolding nanotubes of 8–10 nm in diameter suggesting that these plate-like objects are directly formed by rupture of the nanotubes followed by an unfolding process. However, nanotubes still represent a non-negligible proportion of the nanoparticles present at this temperature of calcination (Fig. 1E).

Calcination at  $600^\circ\text{C}$  leads to a complete loss of the nanotubular morphology of the Na-TNT-600 sample (Fig. 1G). Nanoparticles mostly exhibit non-specified morphology. However, some of them still present a 1D rod-like aspect (Fig. 1H).

### 3.2.2. H-TNT samples before and after calcination

In the case of the H-TNT sample, the complete removal of sodium from the titanate orthorhombic structure did not modify substantially the morphology of the  $\text{TiO}_2$  material. H-TNT is still composed of homogeneous bundles of nanotubes with a diameter of 10–14 nm (Fig. 2) and a wall thickness of 2–3 nm. However, some modifications can also be noticed. First of all, the wall of the nanotubes appeared less crystalline compared to Na-TNT. Close examination of the extremity of one of these nanotubes (Fig. 2C) also shows a rough surface aspect confirming the poor crystallinity of H-TNT.

After calcination at  $400^\circ\text{C}$  for 2 h, the H-TNT-400 sample still presents nanotubular morphology. H-TNT-400 forms assembly of aggregated nanotubes (Fig. 3A and B) resulting in the formation of an inter-granular porosity in the voids formed between aggregated tubes. HRTEM image of the extremity of one of these nanotubes (Fig. 3C) showed that this sample presents open ends with an outer diameter of about 10 nm, an inner diameter of 4 nm and a length of about 100–300 nm. The lattice fringes are more clearly discernable after calcination at  $400^\circ\text{C}$  suggesting a higher crystallinity. An interlayer  $d$  spacing of 0.34 nm can be measured corresponding to the (1 0 1) plane of anatase suggesting that the orthorhombic phase relative to titanate nanotubes was already transformed into anatase at this temperature of calcination.

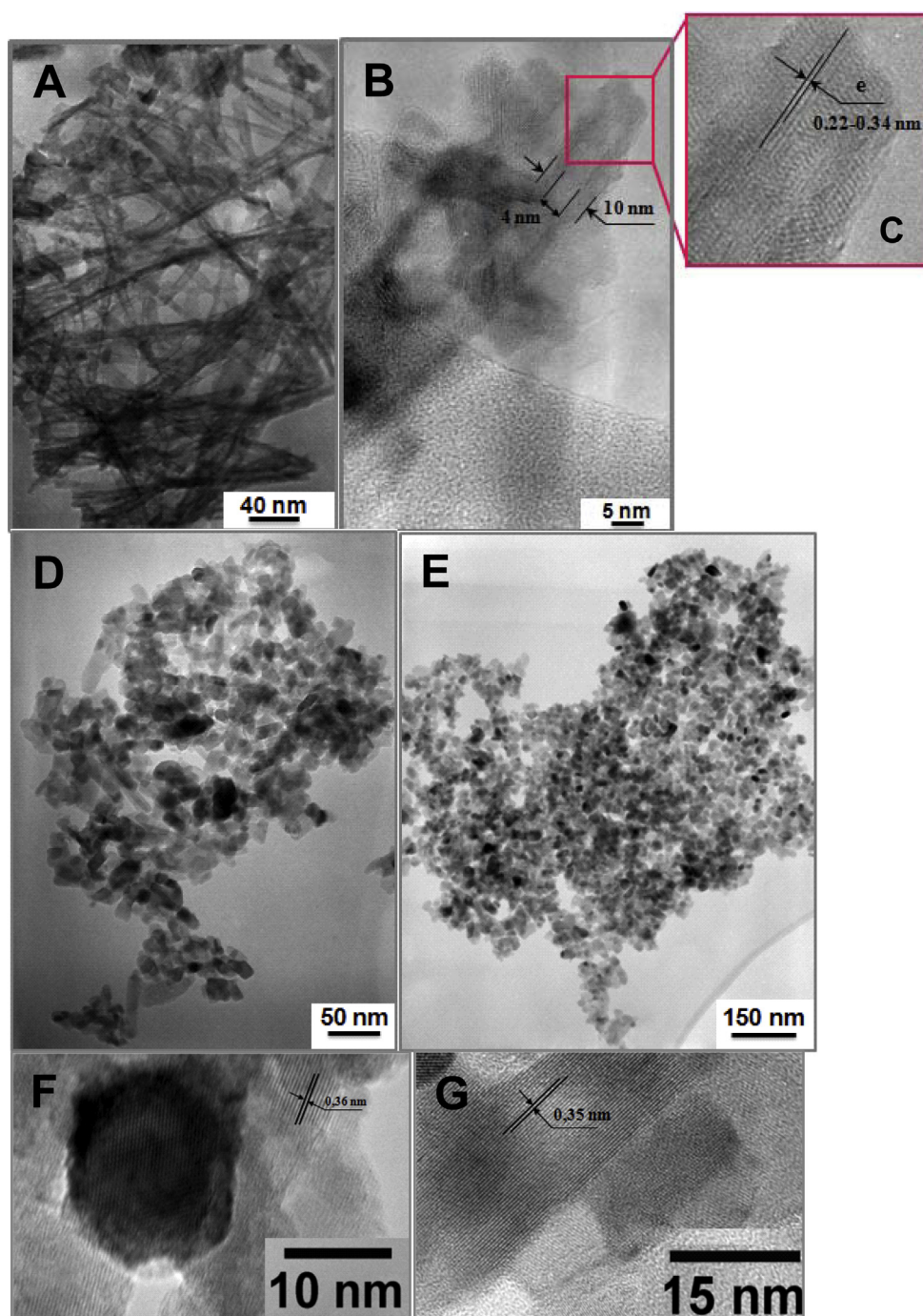


**Fig. 3.** TEM pictures of the H-TNT solid after calcination at 400 °C showing the maintaining of the nanotubular morphology (A–C), and after calcination at 500 °C (D) and at 600 °C (E). HRTEM pictures of the H-TNT-500 (F) and H-TNT-600 (G) are also presented.

After calcination at 500 °C (Fig. 3D), the H-TNT-500 sample has completely lost its monodimensional morphology contrary to Na-TNT-500 leading to the formation of plate-like particles (Fig. 3F). A  $d$  spacing of 0.36 nm can still be measured showing that (1 0 1) planes of anatase can still be detected even after collapse of the nanotubular morphology. After calcination at 600 °C, only agglomerated spherical particles without any precise morphology are obtained (Fig. 3E and G). Noticeably, rod-like objects are not observed. Statistical distributions of the average size of particles obtained on H-TNT-500 and H-TNT-600 showed a progressive increase in size of the  $\text{TiO}_2$  particles due to a sintering phenomenon (Supplementary data Fig. S1).

### 3.3. Textural properties

The nitrogen adsorption-desorption isotherms of the Na-TNT and H-TNT samples before and after calcination are reported in Fig. 4A and B. Whatever the presence or not of sodium in our samples, the initial isotherms of the H-TNT and Na-TNT samples present a type IV profile with H3 hysteresis loops characteristic of non-rigid aggregates of particles giving rise to slit-shaped pores. Therefore, the hydrothermal treatment of the non-porous  $\text{TiO}_2$  P25 leads to the formation of an important porosity. However, the removal of sodium ions also induces a shift to higher  $P/P_0$  relative pressures of the onset of the hysteresis loop showing the presence of larger

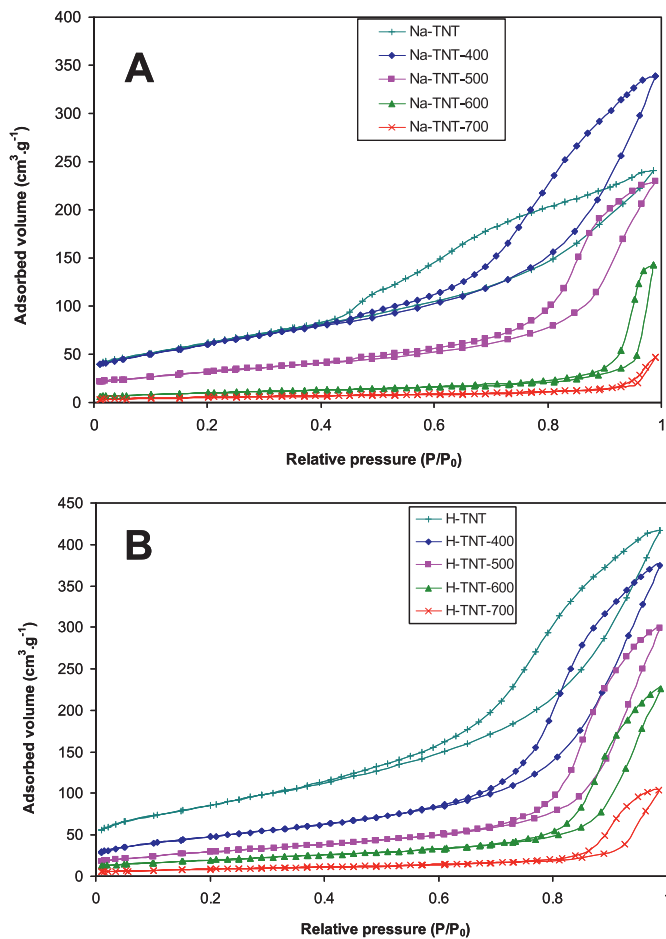


**Fig. 4.**  $N_2$  adsorption–desorption isotherms of the Na-TNT (A) and H-TNT (B) samples before and after calcination.

pores in the H-TNT sample than in Na-TNT. This was confirmed by the BJH pore size distributions of these two samples (Fig. 5A and B). While the Na-TNT sample presents two maxima at 3.5 and 5.0 nm, the H-TNT sample shows a maximum pore size value at 8.0 nm with a shoulder again at 3.5 nm. The smaller pore size maxima observed in both cases could be related to the inner diameter of a nanotubular structure in agreement with TEM results and BET model (cylindrical pores) while the higher pore size maxima are related to intergranular porosity resulting from the natural tendency of this material to form aggregated bunches of particles due to Van der Waals interaction [38,59,63]. Thus, this result suggests that the removal of sodium ions led to a more open assembly of nanotubes with larger interporosity. Determination of the surface areas of H-TNT and Na-TNT (Table 1) also shows an increase of the surface area from  $225 \text{ m}^2 \text{ g}^{-1}$  to  $308 \text{ m}^2 \text{ g}^{-1}$  after removal of sodium. This suggests that the acid washing procedure can liberate some porosity otherwise partially blocked by the presence of residual sodium ions accommodated between the octahedral titania layers [64]. It can also reflect the lower density of the initial titanate nanotube due to the replacement of Na by H [59].

Increasing the temperature of calcination led in both cases to a progressive shift to higher  $P/P_0$  values of the onset of the hysteresis loops which become progressively less marked [30,38,48,65]. However, some differences can also be noted between the calcined samples prepared in the presence or not of sodium. First, the shift to higher  $P/P_0$  values of the onset of the hysteresis loops is more rapid for Na-TNT samples than for H-TNT ones (Fig. 4). This is confirmed by BJH pore size distributions showing that a significant

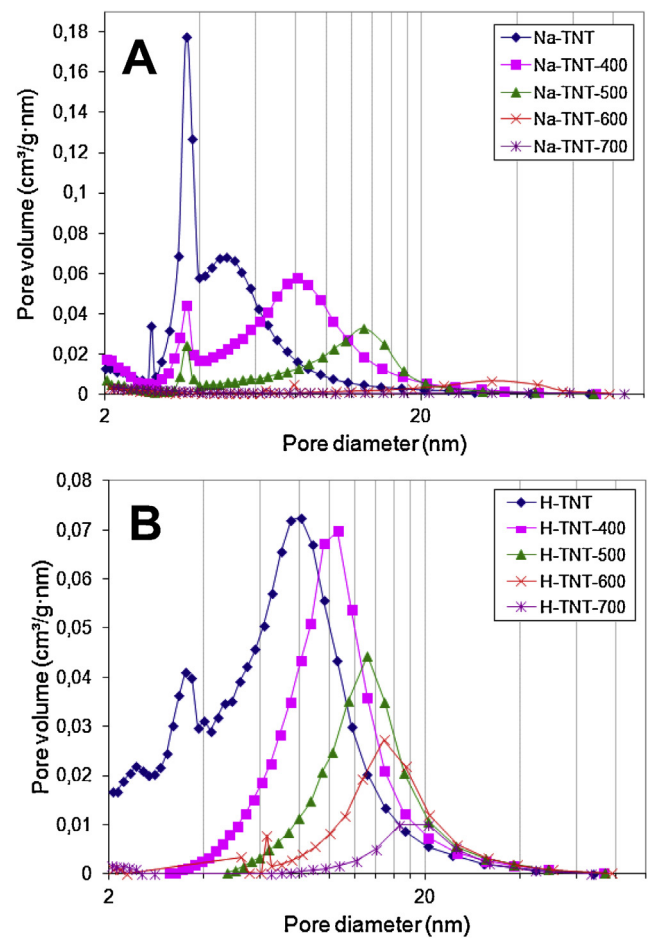


**Fig. 5.** BJH pore size distributions for the Na-TNT (A) and H-TNT (B) samples before and after calcination.

inter-porosity of the H-TNT samples was maintained at higher temperatures of calcination while porosity almost completely collapses at a temperature of calcination of  $700^\circ\text{C}$  for Na-TNT samples (Fig. 5). The lower pore size maximum can still be discerned on Na-TNT samples up to a temperature of calcination of  $500^\circ\text{C}$  while this maximum remains constant at 3.5 nm showing that the nanotubular morphology remains significant up to  $500^\circ\text{C}$  for sodium-containing samples. For H-TNT samples, the pore size maximum at 3.5 nm cannot be observed anymore on samples calcined at  $400^\circ\text{C}$  or higher. This can reflect more probably an overlap of this maximum with the one due to intergranular porosity at least for the sample calcined at  $400^\circ\text{C}$ . However, it also suggests an increase of the inner pore

**Table 1**

Textural properties (specific surface areas and mesoporous pore volumes) and band gap energy values ( $E_g$ ) of the Na-TNT and H-TNT samples before and after calcination. Comparison is given with P25.

Samples	$S_{\text{BET}} (\text{m}^2 \text{ g}^{-1})$	$V_{\text{meso}} (\text{cm}^3 \text{ g}^{-1})$	$E_g (\text{eV}) \pm 0.05 \text{ eV}$
TiO <sub>2</sub> (P25)	50	0.18	3.20
Na-TNT	225	0.54	3.51
Na-TNT-400	221	0.52	3.32
Na-TNT-500	114	0.35	3.23
Na-TNT-600	35	0.22	3.25
Na-TNT-700	18	0.07	3.45
H-TNT	308	0.64	3.31
H-TNT-400	174	0.58	3.17
H-TNT-500	107	0.46	3.19
H-TNT-600	71	0.35	3.17
H-TNT-700	30	0.16	2.94



diameter when increasing temperatures of calcination if samples are removed of their sodium amount.

After calcination at 400 °C, the surface area of the Na-TNT-400 sample remains unchanged at 221 m<sup>2</sup> g<sup>-1</sup> while the H-TNT-400 sample already presents a loss in surface area to 174 m<sup>2</sup> g<sup>-1</sup>, a value 43% lower than for the uncalcined H-TNT sample (Table 1). This result suggests that the presence of sodium also helps in better stabilizing the nanotubular morphology at least at low temperatures of calcinations in good agreement with Qamar *et al.* results [43]. Indeed, for higher temperatures of calcination, the decrease in surface area is more rapid for Na-TNT samples than for H-TNT ones (Table 1). While similar values were found at a temperature of calcination of 500 °C (114 m<sup>2</sup> g<sup>-1</sup> for Na-TNT-500 versus 107 m<sup>2</sup> g<sup>-1</sup> for H-TNT-500), lower values were reached for Na-TNT-600 and Na-TNT-700 than for H-TNT-600 and H-TNT-700 (respectively 35 m<sup>2</sup> g<sup>-1</sup> and 71 m<sup>2</sup> g<sup>-1</sup> at 600 °C, 18 m<sup>2</sup> g<sup>-1</sup> and 30 m<sup>2</sup> g<sup>-1</sup> at 700 °C). Similarly, pore volume values decrease in a similar fashion than surface areas [40]. However, the mixed contribution of inner pore diameter of the nanotubes (when still present) and of the inter-particle voids does not allow ascribing which factor mainly contributes to this decrease in pore volume.

### 3.4. X-ray diffraction

The as-synthesized Na-TNT and H-TNT samples present broad diffraction peaks mainly at 2θ values of 10.0°, 24.6°, 28.4°, and 48.5° which can be ascribed neither to anatase nor to rutile (Supplementary data Figure S2). These XRD patterns correspond to an orthorhombic phase of the type H<sub>2</sub>Ti<sub>2</sub>O<sub>5</sub>·H<sub>2</sub>O (or Na<sub>x</sub>H<sub>2-x</sub>Ti<sub>2</sub>O<sub>5</sub>·H<sub>2</sub>O for Na-TNT) [38,46,66,67]. The main diffraction peaks are then assigned to the (200), (110), (310), (020), and (002) reflections of this orthorhombic phase showing lattice parameters of *a* = 18.03, *b* = 3.78, and *c* = 2.99 Å [68]. Complementary Rietveld analysis of this sample excludes the possibility of formation of the H<sub>2</sub>Ti<sub>3</sub>O<sub>7</sub> phase as reported by other studies [48,59,69]. The (200) peak at 2θ = 10.0° corresponds to the interlayer distance between walls of the nanotubes [46,70].

Comparison of the Na-TNT and H-TNT samples shows a weakening of the intensity of the diffraction peaks after acid washing particularly for the (200) and (310) peaks at 2θ = 10.0° and 28.4° [48,59,71–73] showing a structural transformation induced by the ion-exchange of Na<sup>+</sup> by H<sup>+</sup> ions. However, no shift to higher 2θ values of the (200) peaks was observed during the acid washing showing that the removal of sodium does not influence the interlayer distance between walls of the nanotubes contrary to what was proposed previously [59,66].

The evolution of the XRD patterns of Na-TNT and H-TNT samples with increasing temperature of calcination is reported Fig. 6A–C. Results demonstrate that different levels of sodium initially present in the as-synthesized materials can influence their structural evolution during calcination.

First of all, XRD characterization was first performed at a temperature of calcination of 330 °C corresponding to the first exothermic peak observed by thermal analysis (see further Section 3.6). Interestingly, it can be noticed that the H-TNT-330 sample exhibits an XRD profile presenting broad diffraction peaks with main contributions at 2θ values of 13.5°, 25.3°, 38.2°, 48.5°, 55.0°, and 63.0° (Fig. 6B). Except for the first peak, all these contributions can be assigned to the formation of anatase while the peak at 2θ = 13.5° still reflects the presence of the nanotubular morphology. However, this first rapid observation is insufficient. Indeed, less intense contributions are also detectable at 28.9°, 33.5°, and 44.1°. These weak diffraction peaks show the presence of a TiO<sub>2</sub>(B) contribution in plus of the anatase phase [74]. Other peaks related to the TiO<sub>2</sub>(B) phase would also be expected at 14.2°, 25.0°, 37.8°, 48.6°, 53.2°, 57.4°, and 63.0° but these reflections overlap with

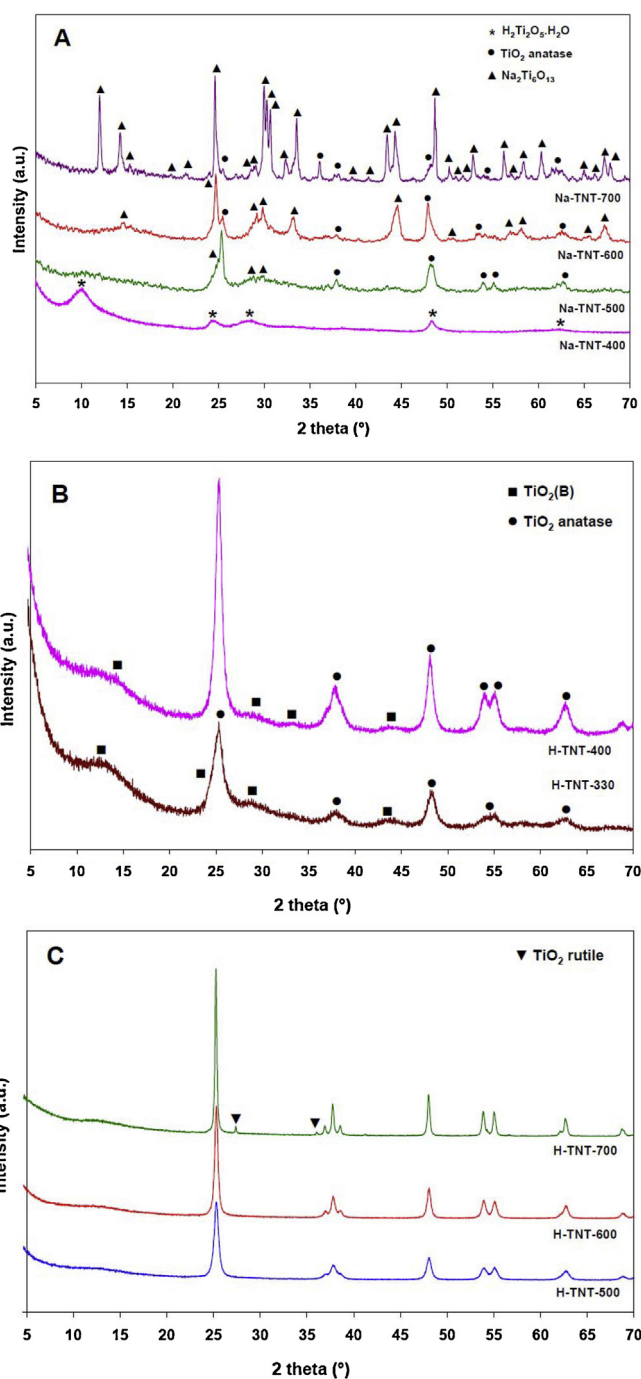


**Fig. 6.** XRD patterns of the Na-TNT samples after calcination (A) and of the H-TNT samples after calcination at 330 °C and 400 °C (B) and after calcination at 500 °C, 600 °C and 700 °C (C).

those coming from anatase or for the 2θ peak at 14.2° with the broad reflection related to the nanotubular morphology. In this latter case, this broad reflection peak presents a shift to higher 2θ values compared to the initial peak detected at 10.0° before calcination. This shift results from a contraction of the interlayer distance between walls of the nanotubes due to a release of water molecules confined in the interlayer spacing [38,71]. Calcination at 330 °C therefore already transforms the initial titanate phase into anatase and/or TiO<sub>2</sub>(B) phases for the samples for which sodium was completely removed. Indeed, on the opposite, the XRD profile of the Na-TNT-330 sample (not shown) does not present any noticeable change compared to the initial Na-TNT sample. However, the exact



proportion of anatase and  $\text{TiO}_2(\text{B})$  cannot be determined due to the poorly crystalline nature of the XRD pattern of H-TNT-330.

After calcination at 400 °C, the Na-TNT-400 sample does not present any noticeable evolution of its diffraction pattern compared to the as-synthesized Na-TNT solid showing that the structure remains unaltered at this temperature of treatment (Fig. 6A).

On the opposite, the H-TNT-400 sample still shows essentially similar contributions than for H-TNT-330 with characteristic diffraction peaks of anatase at  $2\theta$  values of 25.4°, 38.1°, 48.3°, 54.0°, 55.1°, and 62.8° (Fig. 6B).  $\text{TiO}_2(\text{B})$  is still detectable after calcination at 400 °C as reflected by the maintaining of residual weak diffraction peaks of this phase at  $\sim 29.0^\circ$  (002),  $\sim 33.5^\circ$  (310), and  $\sim 44.0^\circ$  (003), other main diffraction peaks overlapping with those of anatase. However, the relative proportions of anatase and  $\text{TiO}_2(\text{B})$  tend to change with the increase of the temperature of calcination from 330 °C to 400 °C. In this respect, the relative ratio of diffraction peak intensities between the  $2\theta$  contribution at  $\sim 25^\circ$  due both to anatase and  $\text{TiO}_2(\text{B})$  and the one at  $\sim 29^\circ$  due only to  $\text{TiO}_2(\text{B})$  can be qualitatively used to evaluate the contributions coming respectively from anatase or from  $\text{TiO}_2(\text{B})$ . Results show that increasing the temperature of calcination from 330 °C to 400 °C results in a 3.5 times higher relative ratio showing a rapid transformation of  $\text{TiO}_2(\text{B})$  into anatase. Moreover, the interlayer distance between walls of the nanotubes keeps showing a progressive contraction of the interlayer distance between walls of the nanotubes as reflected by a further shift of the broad diffraction peak at  $2\theta = 14.2^\circ$ . Its presence otherwise confirms that the nanotubular morphology is still present for the Na-TNT-400 sample as observed by TEM. This interpretation must be however considered once again carefully. Indeed, the presence of a low broad diffraction peak at  $14.2^\circ$  can also be (partly) related to the presence of  $\text{TiO}_2(\text{B})$ . Therefore, the presence of an overlapping diffraction peak of  $\text{TiO}_2(\text{B})$  at  $2\theta$  value of  $14.2^\circ$  limits the possibility to evaluate the effect of calcination at 400 °C on the morphological evolution of the H-TNT-400 sample using XRD.

After calcination at 500 °C, the XRD profile of the Na-TNT-500 sample significantly changes (Fig. 6A). The diffraction peak corresponding to the interlayer distance between walls of the nanotubes is still observed confirming that the nanotubular morphology is preserved even partly after calcination at 500 °C of the Na-TNT sample. However, this peak now slightly shifts to a higher  $2\theta$  value ( $10.7^\circ$ ) showing a small contraction of the layers due to the removal of water confined in the interlayer spacing. These results show that the elimination of water is probably retarded in the present case. However, the exact extent of this retarding effect cannot be definitely determined using only XRD. Results also confirm that the presence of sodium helps to better stabilize the nanotubular morphology at higher temperatures of calcination [71]. The calcination at 500 °C also leads to the appearance of anatase diffraction peaks at  $2\theta$  values of 25.3°,  $\sim 38.0^\circ$ ,  $\sim 48.0^\circ$ ,  $54.0^\circ$ ,  $55.0^\circ$ , and  $62.6^\circ$  ascribed to the (101), (004), (200), (105), (211), and (204) reflections. Moreover, new well-defined peaks can also be observed at  $2\theta$  values of  $24.5^\circ$  and  $\sim 30.0^\circ$ . These peaks are related to the appearance of a still poorly crystallized hexatitanate  $\text{Na}_2\text{Ti}_6\text{O}_{13}$  phase [74].

In the case of the H-TNT-500 sample, the XRD pattern now shows only the presence of the anatase phase which tends to be more crystallized (Fig. 6C). The XRD reflection around  $2\theta \sim 10^\circ$  due to the interlayer distance between walls of a nanotubular structure is not detected anymore confirming the TEM results about the disappearance of the tubular morphology for H-TNT-500.

After calcination at 600 °C, the Na-TNT-600 sample still presents both anatase and the hexatitanate  $\text{Na}_2\text{Ti}_6\text{O}_{13}$  phase (Fig. 6A). However, the intensity of the peaks of the hexatitanate phase tends to increase while oppositely those ascribed to anatase start declining. Calcination at 700 °C confirms this tendency with highly intense  $\text{Na}_2\text{Ti}_6\text{O}_{13}$  diffraction peaks while those attributable to anatase become hardly detected. Rietveld refinement of this last XRD

pattern confirms this assumption with  $\text{Na}_2\text{Ti}_6\text{O}_{13}$  representing 96 wt% of this sample after calcination at 700 °C. This result revealed a progressive transformation of anatase in the presence of a significant amount of residual sodium into the hexatitanate  $\text{Na}_2\text{Ti}_6\text{O}_{13}$  phase.

In the case of the H-TNT samples, calcination at 600 °C did not modify the XRD pattern which still shows an increased crystallization (Fig. 6C). Finally, calcination at 700 °C shows that the anatase phase was still predominating while some weak diffraction peaks of rutile can now be detected at  $2\theta$  values of  $27.4^\circ$  (110) and  $36.1^\circ$  (101). The anatase-to-rutile phase transformation in powder-like aggregated titania samples is known to be a kinetics-controlled process, which becomes significant at  $\text{TiO}_2$  nanoparticle sizes higher than 18 nm [75]. On the other hand, anatase becomes more stable than rutile for titania optimal particle sizes below 14 nm [76]. Our results are in good agreement with these observations:  $\text{TiO}_2$  coherent crystallographic domains (Table 2) increase from 10 nm (H-TNT-400) to 32 nm (H-TNT-700). The crystallinity degree is then accelerated at higher temperatures. The rutile ratio was calculated from the XRD intensity data and results in 5% at 700 °C. Increasing  $\text{TiO}_2$  particle size to 32 nm yields ultimately to rutile phase nucleation. A comparison of anatase particles of size between 7 and 300 nm has indicated a decrease with the size of their thermal stability toward phase transformation into the stable rutile [77].

The textural properties results confirm the aggregation effect under thermal treatment. The specific surface areas of H-TNT samples (Table 1) decreased dramatically, after thermal treatment, due to  $\text{TiO}_2$  nanoparticles aggregation.

### 3.5. Raman spectroscopy

In order to better ascertain the nature of the different phases present at the surface of our samples before and after calcination, Raman spectra were collected for the Na-TNT sample before calcination and for the H-TNT samples before calcination and after calcination at 330 °C, 400 °C, 500 °C, 600 °C, and 700 °C (Fig. 7A and B). The Na-TNT sample presents bands characteristic of titanate nanotubes at 277, 290, 390, 450, 677, 709, 830, and  $926\text{ cm}^{-1}$  assigned to Ti–O lattice vibrations [78–80] (Fig. 7A). Minor contributions also assigned to titanate nanotubes can also be observed at 127, 145, 165, and  $195\text{ cm}^{-1}$  [80]. It should be underlined that the contributions at 145, 195, and  $390\text{ cm}^{-1}$  were assigned previously to the presence of residual anatase [46]. However, this assignment is doubtful here since the  $E_g$  mode of anatase at  $145\text{ cm}^{-1}$  is expected to be the most intense band contrary to what was observed experimentally here. Moreover, Gao et al. reported that hydrogenotitanates can present up to 14 different active Raman modes due to the low symmetry of such compounds with vibration bands at  $145\text{ cm}^{-1}$ ,  $193\text{ cm}^{-1}$ , and  $402\text{ cm}^{-1}$  [79]. Finally, anatase contributions would also then be expected at 519 and  $642\text{ cm}^{-1}$  which are not observed in the present case. Therefore, the Na-TNT sample can be ascribed to a pure titanate phase.

After elimination of sodium, the Raman profile remains essentially similar with still the same characteristic bands of the titanate phase (Fig. 7A). However, a slight red-shift of the bands now at  $271\text{ cm}^{-1}$  ( $-6\text{ cm}^{-1}$  vs Na-TNT) and at  $285\text{ cm}^{-1}$  ( $-5\text{ cm}^{-1}$ ) is observed. Bands were also observed at  $642\text{ cm}^{-1}$  and at  $674\text{ cm}^{-1}$  corresponding to a stronger red-shift of  $35\text{ cm}^{-1}$ . Similar shifts were also observed by Kim et al. [78]. However, the bands initially present at  $390\text{ cm}^{-1}$  and  $450\text{ cm}^{-1}$  blue shift to  $395\text{ cm}^{-1}$  and  $454\text{ cm}^{-1}$  after removal of sodium but in a lower extent suggesting a weak sensitivity to the presence of sodium. Moreover, the bands in the  $550\text{--}750\text{ cm}^{-1}$  range assigned to covalent Ti–O–H bonds tend to become broader on the H-TNT sample. This tendency to broadness can be assigned to higher water content in the H-TNT nanotubular titanate structure. Finally, the band at  $124\text{ cm}^{-1}$  can

**Table 2**

Anatase crystallite size, maximum adsorbed amount of formic acid ( $Q_{\max}$ ), rate constants of degradation ( $k$ ), and  $K$  adsorption constant of formic acid of the different H-TNT samples calcined at different temperatures. Comparison to the P25 as a reference.

Samples	Anatase crystallite sizes (nm)	$Q_{\max}$ ( $\mu\text{mol g}^{-1}$ )	$k$ ( $\mu\text{mol L}^{-1} \text{min}^{-1}$ )	$K$ ( $10^{-3} \text{L } \mu\text{mol}^{-1}$ )
TiO <sub>2</sub> (P25)	19	54	35	8.5
H-TNT-400	10	174	141	1.5
H-TNT-500	14	123	95	2.8
H-TNT-600	18	104	56	4.5
H-TNT-700	32	85	27	8.3

still be observed after complete elimination of sodium. This band was initially assigned by Qian et al. to a Na–O bond [81]. However, its persistence even after removal of sodium definitely rules out this assignment as already suggested by Gajović et al. [80]. Similarly, the band at  $926 \text{ cm}^{-1}$  still persists after complete suppression of sodium. This band cannot then be assigned to bridging Na–O–Ti bonds formed by surface Na on titanate particles [82–85] but more probably to an overtone of the  $450 \text{ cm}^{-1}$  band [78].

After calcination at  $330^\circ\text{C}$ , the Raman profile changed dramatically with a strong intense contribution at  $145 \text{ cm}^{-1}$  due to the  $E_g$  mode of anatase (Fig. 7B). Other anatase vibrations can be observed at  $199 \text{ cm}^{-1}$  ( $E_g$ ),  $400 \text{ cm}^{-1}$  ( $B_{1g}$ ),  $519 \text{ cm}^{-1}$  ( $B_{1g}/A_{1g}$ ), and  $641 \text{ cm}^{-1}$  ( $E_g$ ) [86,87]. However, other lower intense contributions can also be detected at  $123$  (sh),  $172$  (sh),  $238$ ,  $253$ ,  $287$ ,  $365$  (sh), and  $478 \text{ cm}^{-1}$ . These bands are related to the presence of the  $\text{TiO}_2(\text{B})$  phase according to Beuvier et al. [88] and Ben Yahia et al. [89]. Other

contributions of the  $\text{TiO}_2(\text{B})$  phase at  $145$ ,  $196$ , and  $400 \text{ cm}^{-1}$  cannot be observed since overlapping with bands of anatase. Combining these results with those acquired by XRD confirms the presence of  $\text{TiO}_2(\text{B})$  at this temperature of calcination.

Calcination at  $400^\circ\text{C}$  does not modify the Raman signature with still main bands ascribed to the anatase phase. However, the  $\text{TiO}_2(\text{B})$  bands become even weaker suggesting that the transformation of  $\text{TiO}_2(\text{B})$  into anatase is much more advanced after treatment at  $400^\circ\text{C}$ .

At higher temperatures of calcination, the  $\text{TiO}_2(\text{B})$  phase cannot be detected anymore and only anatase is detected in agreement with XRD results.

### 3.6. Thermal analysis

The TGA curves of the H-TNT and Na-TNT materials are reported Fig. 8A. Since only water is expected to be lost during the thermogravimetric analysis, results clearly show that high amount of water was initially present on both samples. This percentage is however higher on the sodium-free H-TNT sample with a loss of  $19.4 \text{ wt}\%$  up to  $600^\circ\text{C}$  versus  $14.8 \text{ wt}\%$  for Na-TNT. This result is in agreement with preceding Raman results showing higher water content on titanate samples when sodium is completely removed. Moreover,

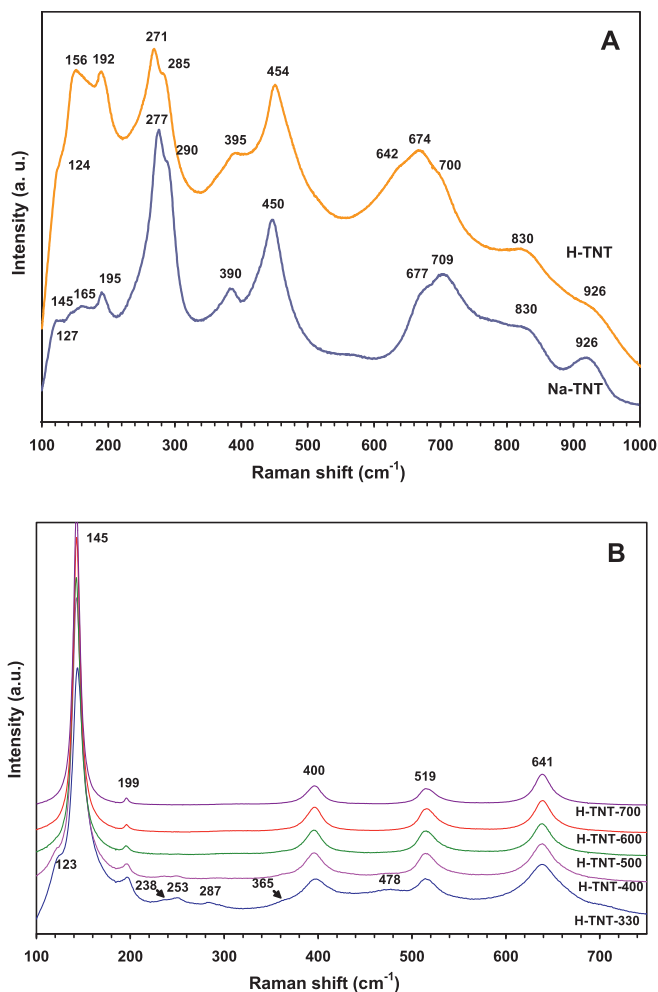


**Fig. 7.** Raman spectra of the Na-TNT and H-TNT samples before calcination (A) and of the H-TNT samples after calcination at  $330$ ,  $400$ ,  $500$ ,  $600$ , and  $700^\circ\text{C}$  (B).

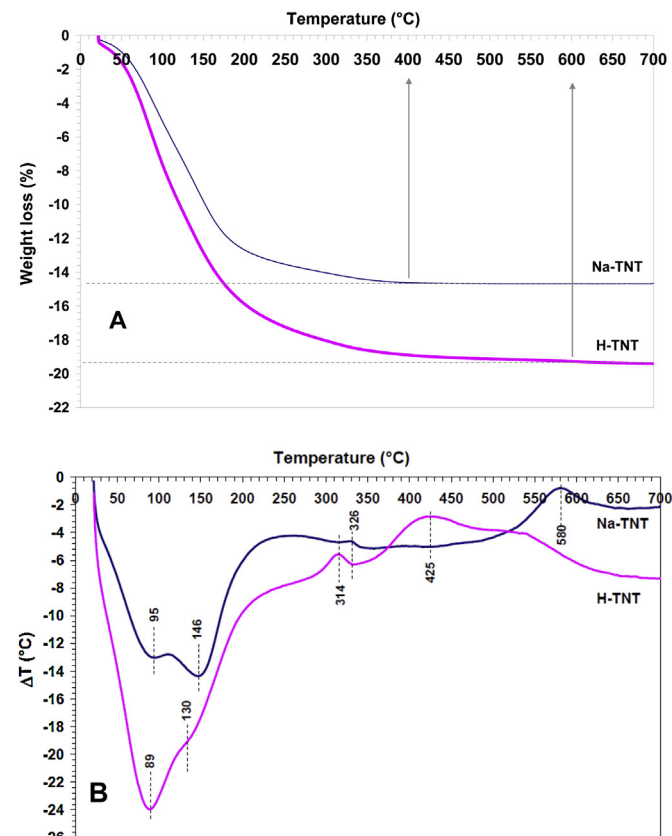


**Fig. 8.** TGA (A) and DTG (B) curves of the Na-TNT and H-TNT samples.

weight stabilization is achieved at a lower temperature (400 °C) for Na-TNT than for H-TNT (600 °C) suggesting a higher stability of the sodium-containing sample. However, this difference remains negligible since the weight loss of the H-TNT sample between 400 °C and 600 °C is only 0.4 wt%.

The DTG curves (Fig. 8B) show the presence of two broad endothermic peaks at 95 °C and 146 °C for Na-TNT and at 89 °C and 130 °C for H-TNT. The first peak is related to adsorbed water during storage and handling due to air moisture [46,59]. Therefore, their relative proportions on the two samples depend mainly on their respective storage conditions and do not bring relevant information about the structural composition of these two samples. One might only notice that the higher surface area of the H-TNT sample would probably favor a higher amount of adsorbed water. The second peak around 130–150 °C can be attributed to the dehydration of interlayered and intralayered OH groups [90]. The broadness of this peak suggests that this dehydration process occurs slowly and is not terminated before 200–250 °C. Above 250 °C, two exothermic peaks can be observed at 326 °C and 580 °C for Na-TNT and at 314 °C and 425 °C for H-TNT. These peaks are related in both cases to the formation of TiO<sub>2</sub>(B) and anatase respectively in agreement with XRD and Raman. TiO<sub>2</sub>(B) is a metastable polymorph formed by dehydration of the layers of the tubular structures of hydrogenotitanates and was appointed as monoclinic TiO<sub>2</sub>. The smaller intensity of the exothermic peak at 326 °C for Na-TNT suggests a lower propensity to form TiO<sub>2</sub>(B) in this case. Moreover, the 150 °C shift to higher temperature of the anatase formation for Na-TNT shows a remarkable effect of sodium in delaying the formation of anatase. Moreover, by subtracting the amount of adsorbed water below 100 °C, it is possible according to Eq. (1) to verify the formation of H<sub>2</sub>Ti<sub>2</sub>O<sub>5</sub> in our H-TNT sample.



The theoretical weight loss due to water removal by dehydration would represent 10.1 wt% if H<sub>2</sub>Ti<sub>2</sub>O<sub>5</sub> was initially present. The experimental weight loss (11.0 wt%) is indeed close to this theoretical value taking into account the uncertainty in determining the real weight loss above 100 °C due to the overlap of the two first DTG peaks. In the case of Na-TNT, taking into account the stoichiometry determined by elemental analysis, the theoretical weight loss would be 8.7 wt% versus 9.2 wt% experimentally confirming once again the presence of an initial Na<sub>x</sub>H<sub>y</sub>Ti<sub>2</sub>O<sub>5</sub> (or H<sub>2</sub>Ti<sub>2</sub>O<sub>5</sub>) stoichiometry.

### 3.7. Diffuse reflectance UV–vis characterization

The diffuse reflectance UV–vis spectra of H-TNT and Na-TNT samples are dominated by the strong absorption of titanate solids in the UV region. However, a significant shift to longer wavelength is observed when removing sodium from the titanate structure (Supplementary data Fig. S3A). To determine the band gap energy ( $E_g$ ) of the samples, the Kubelka–Munk method was used.  $(F(R)hv)^{1/2}$  versus  $h\nu$  plots were built with  $F(R) = (1 - R)/2R$  in order to determine  $E_g$  values. Results are reported in Table 1. The removal of exchangeable sodium from the nanotubular titanate moves the energy gap from 3.51 to 3.31 eV. This value is slightly higher than the one reported for anatase (3.23 eV) [46]. However, this difference is only marginal when sodium is completely removed from the nanotubes.

Calcination of the Na-TNT sample leads to a red shift of the diffuse reflectance UV–vis spectra as soon as the temperature is increased to 400 °C (Supplementary data Fig. S3B). This red shift is even more significant after treatment at 500 °C while oppositely a blue shift is observed after calcination at 600 °C and 700 °C. This evolution was confirmed when calculating their respective  $E_g$  values. Calcination at 400 °C reduces the band gap from 3.51 eV to

3.32 eV while  $E_g$  values close to the one expected for anatase are observed after calcination at 500 °C and 600 °C. This result is in agreement with XRD results showing the presence of the anatase phase at these temperatures of calcination. The  $E_g$  value increases after calcination at 700 °C ( $E_g = 3.45$  eV) probably in agreement with the formation at this temperature of the hexatitanate phase.

Calcination of the H-TNT sample also leads to a red shift of the diffuse reflectance UV–vis spectra as soon as 400 °C while no significant shift can be observed after calcination up to 600 °C (Supplementary data Fig. S3C). Calcination at 700 °C leads to a more important red shift with a tail slightly extending into the visible region. This evolution leads to only a moderate decrease of the band gap value to 3.17–3.19 eV as soon as calcination at 400 °C. No detectable evolution can be observed up to 600 °C reflecting probably the presence of only anatase at these temperatures of treatment. A significant decrease to 2.94 eV can however be noticed after calcination at 700 °C linked probably to the presence of some rutile phase [91] as also detected by XRD. These results therefore are consistent with those observed previously with the Na-TNT sample evolving to anatase and then to the hexatitanate phase while the H-TNT phase forms almost exclusively anatase.

### 3.8. Role of sodium toward structural and morphological transformation of titanate nanotubes

The characterization results clearly emphasize the main role of sodium in terms of structural and morphological transformation. First of all, TEM studies clearly emphasize that the presence of sodium allows maintaining the nanotubular morphology up to 500 °C versus 400 °C in the absence of sodium. However, results also clearly show that the complete sodium removal does not provoke any collapse of the nanotubular morphology contrary to the results of Lee et al. [48]. In fact, the presence of sodium tends to control the rate of dehydration of the initial titanate phase with a slightly more rapid process in the absence of sodium. For H-TNT samples, dehydration leads to the formation of TiO<sub>2</sub>(B) after calcination at 330 °C. However, already at this temperature, even if the bulk phase is TiO<sub>2</sub>(B), anatase surface domains starts being present on the surface of the nanotubes. On the opposite, in the presence of sodium, the formation of the anatase phase is retarded. However, the simultaneous presence of residual sodium does not allow obtaining a pure anatase phase. Indeed, anatase rapidly reacts with sodium to form almost uniquely the hexatitanate phase, Na<sub>2</sub>Ti<sub>6</sub>O<sub>13</sub> at high temperature of calcination. Once again, the end of the dehydration process does not coincide neither with the formation of an anatase phase (TiO<sub>2</sub>(B) is formed first) nor with the loss of the nanotubular morphology. However, once the anatase phase is obtained, the temperature range in which the nanotubular morphology can be maintained remains relatively narrow ( $\sim \Delta T = 100$  °C) showing an intrinsic instability of nanotubes walls [59].

### 3.9. Photocatalytic degradation of formic acid

#### 3.9.1. Effect of sodium and calcination temperature on the formic acid degradation

The activity of the Na-TNT and H-TNT samples calcined at different temperatures has therefore been evaluated in the photocatalytic oxidation of formic acid (FA). Fig. 9 shows the evolution of the amount of formic acid in solution ( $[\text{FA}]_0 = 50 \text{ mg L}^{-1} = 1087 \mu\text{mol L}^{-1}$ ) in the dark and with UV illumination. For comparison purposes, the photocatalytic activity of a P25 reference was also determined under identical conditions. Adsorption equilibrium was first acquired under dark conditions during 30 min (“UV OFF”). Results only show a negligible decrease of the FA concentration by adsorption of formic acid on the surface of the different photocatalysts. UV illumination was then



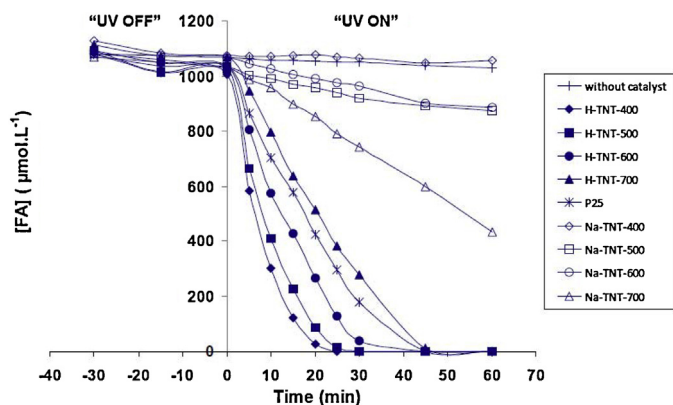


**Fig. 9.** Evolution with time of the concentration of formic acid in solution using Na-TNT and H-TNT samples calcined at different temperatures under dark and UV-illuminated conditions ( $[\text{FA}] \approx 50 \text{ mg L}^{-1} \approx 1087 \mu\text{mol L}^{-1}$ ;  $V = 30 \text{ mL}$ ;  $[\text{TiO}_2] = 1 \text{ g L}^{-1}$ ; natural  $\text{pH} \approx 3$ ). Comparison is provided with the P25 reference.

performed during 1 h ("UV ON"). In the absence of a photocatalyst, the FA concentration hardly changes showing that photolysis degradation of formic acid did not occur under our experimental conditions. Results also clearly evidence a very different comportment between the Na-TNT and H-TNT samples. Na-TNT samples presenting significant amount of sodium exhibit much lower photocatalytic activities than their H-TNT counterparts for all the different calcination temperatures. Interestingly, the Na-TNT-400 sample appears almost completely inactive toward formic acid photodegradation. Since XRD results have shown that calcination at  $400^\circ\text{C}$  did not alter the initial as-formed titanate phase, this result shows the inefficacy of the titanate phase particularly when sodium is present.

Increasing the calcination temperature to  $500^\circ\text{C}$  and to  $600^\circ\text{C}$  leads to low degradation rate, while further increase of the temperature of calcination to  $700^\circ\text{C}$  involves a meaningful improvement of the degradation rate of formic acid. These last results can be interpreted considering previous XRD results. After calcination at  $500^\circ\text{C}$  and  $600^\circ\text{C}$ , the initial orthorhombic titanate structure has been transformed first into anatase while the substantial amount of residual sodium starts reacting with anatase to form the hexatitanate phase,  $\text{Na}_2\text{Ti}_6\text{O}_{13}$ . If anatase is well-known to be photocatalytically active, the presence of residual sodium favors the formation of surface and bulk recombination centers of photogenerated  $e^-h^+$  pairs [92–94]. Interestingly, increasing the temperature of calcination to  $700^\circ\text{C}$  leads to an improvement of the photocatalytic activity. Several factors can be considered when explaining the variation in photocatalytic activity observed after calcination at  $700^\circ\text{C}$  like the proportion of anatase phase, its crystallinity, or the surface area, this last parameter being ambiguous since also known to provide sometimes a higher proportion of recombination centers. However, the proportion of anatase phase after calcination at  $700^\circ\text{C}$  is quite low as determined from XRD patterns by Rietveld refinement (4 wt%) while the surface area is only  $18 \text{ m}^2 \text{ g}^{-1}$ . A more reasonable explanation about the Na-TNT-700 photoactivity would be indirectly related to the almost complete transformation of the anatase phase into  $\text{Na}_2\text{Ti}_6\text{O}_{13}$ . Indeed, this complete transformation implies that almost all the residual sodium has then reacted with anatase to form the hexatitanate phase limiting its negative influence.

Strikingly, the complete removal of sodium leads to much higher photocatalytic activities for the H-TNT samples confirming the role of sodium as recombination centers. In this respect, the HNT sample calcined at  $400^\circ\text{C}$  and still showing nanotubular morphology presents the best photocatalytic activity. Indeed, with H-TNT-400, complete degradation of formic acid is achieved in about 25 min.

For comparison, using P25, complete degradation is only obtained after 45 min. Increasing the temperature of calcination results in a progressive decrease of the photocatalytic activity. This decrease remains moderate after calcination at  $500^\circ\text{C}$  and  $600^\circ\text{C}$  still leading to photocatalytic samples more active than P25. Further increase of the temperature of calcination to  $700^\circ\text{C}$  leads to a more marked decrease of the photocatalytic activity with the H-TNT-700 sample degrading formic acid more slowly than P25. To better emphasize the causes explaining the highest photocatalytic activity achieved with H-TNT-400, the following sections will be centered on the determination of the adsorption isotherms and on the kinetic analysis of the most active series of samples, i.e. the H-TNT series.

### 3.9.2. Adsorption isotherms of formic acid

The amount of formic acid adsorbed in the dark per gram of catalyst ( $Q_e$ ) is reported in Supplementary data Fig. S4 as a function of the formic acid concentration present in solution ( $C_e$ ) for the H-TNT samples. These adsorption isotherm curves of formic acid can be modeled using a Langmuir model. The maximum adsorbed amount of formic acid ( $Q_{\text{max}}$ ) can therefore be determined by the method of the least-squares fitting according to the Eq. (2).

$$\frac{Q_{\text{ads}}}{Q_{\text{max}}} = \frac{K_{\text{ads}} C_e}{1 + K_{\text{ads}} C_e} \quad (2)$$

where  $Q_{\text{ads}}$  is the adsorbed quantity of formic acid,  $K_{\text{ads}}$  is the adsorption constant, and  $C_e$  is the concentration of FA at the adsorption equilibrium.

Results reported in Table 2 reveal a strong evolution of the maximum amount of formic acid to be adsorbed from  $174 \mu\text{mol g}^{-1}$  for H-TNT-400 to  $85 \mu\text{mol g}^{-1}$  for H-TNT-700. For comparison, on P25,  $Q_{\text{max}}$  reaches a value of  $54 \mu\text{mol g}^{-1}$ .

Coverage rates ( $\theta = Q_{\text{ads}}/Q_{\text{max}}$ ) can therefore be obtained in function of  $C_e$  for the different solids studied here (Supplementary data Fig. S5). At the initial FA concentration of  $50 \text{ mg L}^{-1}$  ( $1087 \mu\text{mol L}^{-1}$ ) as shown in Fig. 9, it can be observed that only 60% of the H-TNT-400 surface is covered during the photocatalytic reaction while the coverage rate reaches values between 75% and 90% for other samples. This finding suggests that the higher intrinsic activity of the H-TNT-400 sample is directly related to a lower surface saturation by formic acid during reaction probably related to the high specific surface area of this nanotubular  $\text{TiO}_2$  solid.

### 3.9.3. Langmuir–Hinshelwood kinetics

The determination of the initial rate ( $r_0$ ) of degradation at different initial concentrations of FA for each material allows representing the kinetic behavior of the FA photocatalytic degradation. The instantaneous rate at 5 min of reaction is here considered to be the initial rate  $r_0$ . The initial rate of degradation ( $r_0$ ) in function of FA concentration present in solution is reported in Fig. 10. At low concentrations of FA, the initial rate of degradation increases proportionally as a function of the FA concentration in solution. Further increase of the FA concentration above  $400 \mu\text{mol L}^{-1}$  leads to a progressive level off of all the curves while a plateau is reached above  $4000 \mu\text{mol L}^{-1}$ . A noticeable exception is the H-TNT-400 sample still presenting a moderate increase of  $r_0$  above  $4000 \mu\text{mol L}^{-1}$  probably due to its high surface area limiting the saturation of the surface by the reactant contrary to other samples.

These curves can therefore be normalized using a Langmuir–Hinshelwood model according to the Eq. (3).

$$r_0 = \frac{k K C_e}{1 + K C_e} \quad (3)$$

where  $r_0$  is the initial rate of degradation,  $k$  is the rate constant for formic acid degradation, and  $K$  the adsorption constant of formic acid.

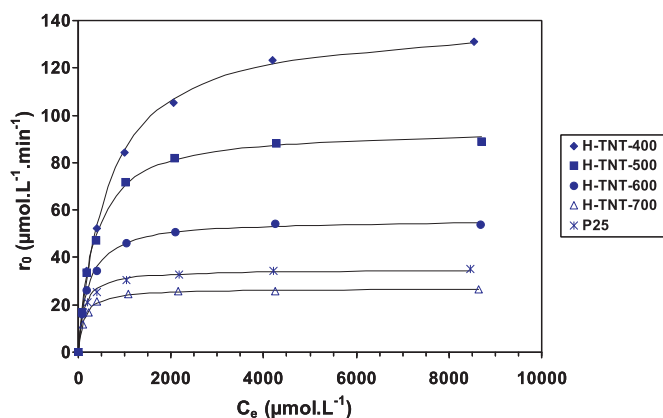


**Fig. 10.** Evolution of the initial rates of degradation  $r_0$  as a function of the concentration of formic acid at the adsorption equilibrium,  $C_e$  for the different H-TNT samples calcined at different temperatures. Comparison is provided with the P25 reference. Symbols refer to experiment values and curves to the Langmuir–Hinshelwood model.

Results about rate constants for each material are reported in Table 2. The nanotubular sample obtained after calcination at 400 °C (H-TNT-400) presents a rate constant ( $141 \mu\text{mol.L}^{-1}.\text{min}^{-1}$ ) four times higher than P25 ( $35 \mu\text{mol.L}^{-1}.\text{min}^{-1}$ ). However, increasing the calcination temperature leads to a progressive decrease of the rate constant from  $95 \mu\text{mol.L}^{-1}.\text{min}^{-1}$  for H-TNT-500 to  $56 \mu\text{mol.L}^{-1}.\text{min}^{-1}$  for H-TNT-700. This last photocatalyst however still presents a rate constant value 60% higher than P25.

The determination of the adsorption constants of formic acid shows on the opposite a marked increase with increasing temperature of calcination (Table 2) from  $1.5 \times 10^{-3} \text{L}.\mu\text{mol}^{-1}$  for H-TNT-400 to  $8.3 \times 10^{-3} \text{L}.\mu\text{mol}^{-1}$  for H-TNT-700. In agreement with the higher coverage rates observed with increasing calcination temperatures, this result shows a higher tendency of adsorbing more strongly formic acid with the increase of the anatase crystallization degree consecutively to the calcination treatment. This result combined with the loss of surface area will favor an even more marked surface saturation by the reactant with increasing temperature of calcination disfavoring the photocatalytic activity.

### 3.9.4. Correlation between photocatalytic activity and textural and structural properties

For all the H-TNT samples calcined between 400 °C and 700 °C, a direct correlation between the rate constant and the specific surface area can be observed (Fig. 11A). This shows that, in the particular case of the formic acid degradation, the increase of surface area allows a higher amount of formic acid to be adsorbed impacting directly its further photodegradation. However, this enhancement of the textural properties is not the only important parameter here. Indeed, for the H-TNT sample calcined at 330 °C, even if a very high specific surface area is reached ( $265 \text{m}^2 \text{g}^{-1}$ ), the corresponding rate constant is much lower ( $48 \mu\text{mol.L}^{-1}.\text{min}^{-1}$ ) and does not fit with the linear correlation observed from H-TNT-400 to H-TNT-700. This shows that the nature of the phase present also plays an important role: in the case of H-TNT-330, the presence of a significant amount of  $\text{TiO}_2(\text{B})$  influences negatively the photocatalytic properties. On the opposite, these results also show the importance of combining increased surface area and anatase formation. Fig. 11 also underlines that the formation of  $\text{TiO}_2$  anatase nanotubes for H-TNT-400 leads to an enhanced photocatalytic activity. However, this improvement only results from the higher surface accessibility to reactant both inside and outside the nanotubes. The fact that the rate constant was directly proportional to the specific surface area whatever the morphology of the H-TNT anatase samples also shows that the nanotubular morphology is

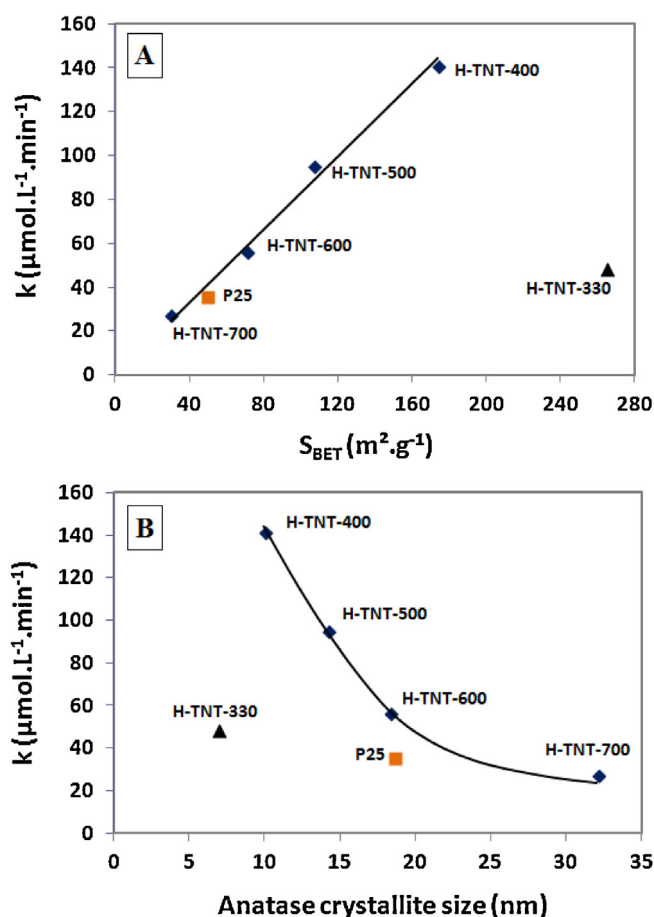


**Fig. 11.** (A) Correlation between the rate constant for formic acid degradation ( $k$ ) and the specific surface area of the H-TNT samples. (B) Correlation between the rate constant for formic acid degradation ( $k$ ) and  $\text{TiO}_2$  particle size. Comparison is provided with the H-TNT sample calcined at 330 °C (H-TNT-330) comprising a significant amount of  $\text{TiO}_2(\text{B})$  and with the P25 reference.

interesting in this case but only by providing a higher surface area while the anatase phase is already formed. This higher surface area combined with a lower reactant adsorption constant allows degrading readily formic acid on H-TNT-400. This result also means that the anisotropy shape by itself does not provide any intrinsic enhancement through more efficient charge carrier separation in this particular case.

An analysis of different factors that affect the material activity is very difficult because of their coupling. In particular, the particle size can also strongly affect its crystalline quality and phase. Fig. 11 B also underlines a more suitable correlation between the rate constant and  $\text{TiO}_2$  coherent crystallographic domains. Our results show clearly that the photodegradation of formic acid decreases by increasing  $\text{TiO}_2$  crystallinity. A comparison with HNT-330 sample, presenting the smallest  $\text{TiO}_2$  particle size (7 nm), shows clearly the effect of the crystalline quality of anatase. DRX results (Fig. 6B) showed the presence of not well crystallized anatase and  $\text{TiO}_2(\text{B})$  phases. At same  $\text{TiO}_2$  particle size (18 nm), the intrinsic activities of P25 and H-TNT-600 samples are quite similar. This suggests that H-TNT-600 sample, formed only of anatase, can provide similar amount of sites per  $\text{cm}^2$  with respect to P25 even if P25 is a mixture of anatase and rutile.

Therefore, in order to achieve a high photodegradation activity: a good crystalline quality of anatase phase and coherent crystallographic domains of  $\text{TiO}_2$  must be fulfilled.

Finally, we should keep in mind that such a result, valid for formic acid, cannot be easily generalized to other pollutants to

be degraded and that future studies are still necessary to better apprehend the photocatalytic mechanism relevant for a particular pollutant to be degraded.

#### 4. Conclusion

The influence of sodium on the textural, structural, morphological and photocatalytic properties of hydrogenotitanates nanotubes calcined at different temperatures has been extensively studied in the present work. Results show that the elaborated nanotubes contain huge amount of water and consist of titanates having an orthorhombic structure with formula  $\text{Na}_{2-x}\text{H}_x\text{Ti}_2\text{O}_5 \cdot n\text{H}_2\text{O}$  and  $\text{H}_2\text{Ti}_2\text{O}_5 \cdot n\text{H}_2\text{O}$ , where  $x$  depending on the washing process with acid. Phase structure, morphology, specific surface area and pores distribution strongly depend on the sodium content and the calcination temperature. Results demonstrate that sodium mainly influences the structural transformation of titanate into anatase through a slower dehydration process shifting to higher temperature the transformation of titanate into anatase. However, the presence of sodium is not a pre-requisite for preserving the nanotubular morphology. Indeed, the end of the dehydration process does not correspond neither to the formation of only anatase nor to the breaking of the nanotubes. Sodium also hinders the formation of pure anatase samples since residual sodium coming from the initial titanate phase tends to readily react with anatase to form a hexatitanate phase.

The influence of sodium on photocatalytic properties has also been analyzed. At low calcination temperature ( $<500^\circ\text{C}$ ), the Na-TNT nanotubes were found to be inert toward the photocatalytic degradation of FA showing the role of sodium as recombination centers for photogenerated electron-hole pairs. In this respect, removal of sodium through 1 M acid washing treatment followed by calcination allows increasing markedly photocatalytic activity. Such an approach led in the case of the H-TNT-400 sample formed of  $\text{TiO}_2$  anatase nanotubes to a photocatalyst 4 times more active than P25 for the degradation of formic acid. Determination of adsorption isotherms and kinetic parameters reveal that the high photocatalytic activity achieved by the H-TNT-400 sample results from the high surface area of this anatase sample which combined with a lower adsorption constant of formic acid allows avoiding surface saturation by the reactant and therefore loss of activity. Therefore, in order to achieve a high photodegradation activity of formic acid, a high surface area of  $\text{TiO}_2$  anatase (well crystalline) nanomaterial with small coherent crystallographic domains must be fulfilled.

#### Acknowledgments

This work was supported by the Agence Universitaire de la Francophonie (AUF). The AUF and IRC Lyon of the University Claude Bernard are greatly acknowledged.

#### Appendix A. Supplementary data

Supplementary data associated with this article can be found, in the online version, at <http://dx.doi.org/10.1016/j.apcatb.2013.03.020>.

#### References

- [1] D.V. Bavykin, J.M. Friedrich, F.C. Walsh, *Advanced Materials* 18 (2006) 2807–2824.
- [2] T. Kasuga, *Thin Solid Films* 496 (2006) 141–145.
- [3] X.F. Xiao, T. Tian, R.F. Liu, H.D. She, *Materials Chemistry and Physics* 106 (2007) 27–32.
- [4] S.H. Oh, R.R. Finones, C. Daraio, L.H. Chen, S. Jin, *Biomaterials* 26 (2005) 4938–4943.
- [5] H. Zhang, X.P. Ga, G.R. Li, T.Y. Yan, H.Y. Zhu, *Electrochimica Acta* 53 (2008) 7061–7068.
- [6] J. Li, Z. Tang, Z. Zhang, *Electrochemistry Communications* 7 (2005) 62–67.
- [7] J. Li, Z. Tang, Z. Zhang, *Chemical Physics Letters* 418 (2006) 506–510.
- [8] E.A. Kozlova, A.V. Vorontsov, *Applied Catalysis B* 77 (2007) 35–45.
- [9] R.J. Tayade, P.K. Surolia, R.G. Kulkarni, R.V. Jasra, *Science and Technology of Advanced Materials* 8 (2007) 455–462.
- [10] S.J. Tsai, S. Cheng, *Catalysis Today* 33 (1997) 227–237.
- [11] C.H. Hana, D.W. Honga, I.J. Kima, J. Gwak, S.D. Hana, K.C. Singh, *Sensors and Actuators B* 128 (2007) 320–325.
- [12] D.U. Hong, C.H. Han, S.H. Park, I.J. Kim, J. Gwak, S.D. Han, H.J. Kim, *Current Applied Physics* 9 (2009) 172–178.
- [13] C.H. Lin, C.H. Lee, J.H. Chao, C.Y. Kuo, Y.C. Cheng, W.N. Huang, H.W. Chang, Y.M. Huang, M.K. Shih, *Catalysis Letters* 98 (2004) 61–66.
- [14] G.H. Du, Q. Chen, R.C. Che, Z.Y. Yuan, L.M. Peng, *Applied Physics Letters* 79 (2001) 3702–3704.
- [15] M. Wang, D.J. Guo, H.L. Li, *Journal of Solid State Chemistry* 178 (2005) 1996–2000.
- [16] L.M. Sikkhivilu, N.J. Coville, D. Nares, K.V.R. Chary, V. Vishwanathan, *Applied Catalysis A* 324 (2007) 52–61.
- [17] J. Yu, H. Yu, B. Cheng, X. Zhao, Q. Zhang, *Journal of Photochemistry and Photobiology A* 182 (2006) 121–127.
- [18] G.S. Guo, C.N. He, Z.H. Wang, F.B. Gu, D.M. Han, *Talanta* 72 (2007) 1687–1692.
- [19] M. Inagaki, N. Kondo, R. Nonaka, E. Ito, M. Toyoda, K. Sogabe, T. Tsumura, *Journal of Hazardous Materials* 161 (2009) 1514–1521.
- [20] J.C. Hulteen, C.R. Martin, *Journal of Materials Chemistry* 7 (1997) 1075–1087.
- [21] A. Michailowski, D. Al-Mawlawi, G.S. Cheng, M. Moskovits, *Chemical Physics Letters* 349 (2001) 1–5.
- [22] S.Z. Chu, K. Wada, S. Inoue, S.I. Todoroki, *Chemistry of Materials* 14 (2002) 266–272.
- [23] D. Gong, C.A. Grimes, O.K. Varghese, W. Hu, R.S. Singh, Z. Chen, E.C. Dickey, *Journal of Materials Research* 16 (2001) 3331–3334.
- [24] H. Tsuchiya, J.M. Macak, L. Taveira, E. Balaur, A. Ghicov, K. Sirotna, P. Schmuki, *Electrochemistry Communications* 7 (2005) 576–580.
- [25] T. Kasuga, M. Hiramatsu, A. Hoson, T. Sekino, K. Niihara, *Langmuir* 14 (1998) 3160–3163.
- [26] Y. Lan, X. Gao, H. Zhu, Z. Zheng, T. Yan, F. Wu, S.P. Ringer, D. Song, *Advanced Functional Materials* 15 (2005) 1310–1318.
- [27] T. Kasuga, M. Hiramatsu, A. Hoson, T. Sekino, K. Niihara, *Advanced Materials* 11 (1999) 1307–1311.
- [28] H. Kochkar, N. Lakhdhar, G. Berhault, M. Bausach, A. Ghorbel, *Journal of Physical Chemistry C* 113 (2009) 1672–1679.
- [29] H.H. Ou, S.L. Lo, *Separation and Purification Technology* 58 (2007) 179–191.
- [30] Z.Y. Yuan, B.L. Su, *Colloids and Surfaces A* 241 (2004) 173–183.
- [31] R. Yoshida, Y. Suzuki, S. Yoshikawa, *Materials Chemistry and Physics* 91 (2005) 409–416.
- [32] D.V. Bavykin, A.N. Kulak, F.C. Walsh, *Crystal Growth and Design* 10 (2010) 4421–4427.
- [33] C.L. Wong, Y.N. Tan, A.R. Mohamed, *Journal of Environment Management* 92 (2011) 1669–1680.
- [34] W. Wang, O.K. Varghese, M. Paulose, C.A. Grimes, Q. Wang, E.C. Dickey, *Journal of Materials Research* 19 (2004) 417–422.
- [35] Q. Chen, G.H. Du, S. Zhang, L.-M. Peng, *Acta Crystallographica B* 58 (2002) 587–593.
- [36] A. Nakahira, W. Kato, M. Tamai, T. Isshiki, K. Nishio, H. Aritani, *Journal of Materials Science* 39 (2004) 4239–4245.
- [37] J. Yang, Z. Jin, X. Wang, W. Li, J. Zhang, S. Zhang, X. Guo, Z. Zhang, *Dalton Transactions* 33 (2003) 3898–3901.
- [38] B. Vijayan, N.M. Dimitrijevic, T. Rajh, K. Gray, *Journal of Physical Chemistry C* 114 (2010) 12994–13002.
- [39] S. Ribbens, I. Caretti, E. Beyers, S. Zamani, E. Vinck, S.V. Doorslaer, P. Cool, *Journal of Physical Chemistry C* 115 (2011) 2302–2313.
- [40] J. Yu, H. Yu, B. Cheng, C. Trapalis, *Journal of Molecular Catalysis A: Chemical* 249 (2006) 135–142.
- [41] N. Xiao, Z. Li, J. Liu, Y. Gao, *Thin Solid Films* 519 (2010) 541–548.
- [42] S. Mozia, *Catalysis Today* 156 (2010) 198–207.
- [43] M. Qamar, C.R. Yoon, H.J. Oh, N.H. Lee, K. Park, D.H. Kim, K.S. Lee, W.J. Lee, S.J. Kim, *Catalysis Today* 131 (2008) 3–14.
- [44] H. Yu, J. Yu, B. Cheng, *Chemosphere* 66 (2007) 2050–2057.
- [45] J. Jitputti, Y. Suzuki, S. Yoshikawa, *Catalysis Communications* 9 (2008) 1265–1271.
- [46] S. Mozia, E. Borowiak-Paleń, J. Przepiórski, B. Grzmil, T. Tsumura, M. Toyoda, J. Grzechulska-Damszel, A.W. Morawski, *Journal of Physics and Chemistry of Solids* 71 (2010) 263–272.
- [47] M. Zhang, Z. Jin, J. Zhang, X. Guo, J. Yang, W. Li, X. Wang, Z. Zhang, *Journal of Molecular Catalysis A: Chemical* 217 (2004) 203–210.
- [48] C.K. Lee, C.C. Wang, M.D. Lyu, L.C. Juang, S.S. Liu, S.H. Hung, *Journal of Colloid and Interface Science* 316 (2007) 562–569.
- [49] V. Bem, M.C. Neves, M.R. Nunes, A.J. Silvestre, O.C. Monteiro, *Journal of Photochemistry and Photobiology A* 232 (2012) 50–56.
- [50] M. Mrowetz, E. Selli, *Journal of Photochemistry and Photobiology A* 180 (2006) 15–22.
- [51] T. An, Y. Xiong, G. Li, C. Zha, X. Zhu, *Journal of Photochemistry and Photobiology A* 152 (2002) 155–165.
- [52] D.S. Muggli, M.J. Backes, *Journal of Catalysis* 209 (2002) 105–113.
- [53] L. Davydov, P.G. Smirniotis, *Journal of Catalysis* 191 (2000) 105–115.



- [54] I. Mazzarino, P. Piccinini, *Chemical Engineering Science* 54 (1999) 3107–3111.
- [55] M. Bideau, B. Claudel, M. Otterbein, *Journal of Photochemistry* 14 (1980) 291–302.
- [56] H. Kochkar, A. Turki, L. Bergaoui, G. Berhault, A. Ghorbel, *Journal of Colloid and Interface Science* 331 (2009) 27–31.
- [57] A. Turki, H. Kochkar, G. Berhault, A. Ghorbel, *Studies in Surface Science and Catalysis* 175 (2010) 593–596.
- [58] B. Poudel, W.Z. Wang, C. Dames, J.Y. Huang, S. Kunwar, D.Z. Wang, D. Banerjee, G. Chen, Z.F. Ren, *Nanotechnology* 16 (2005) 1935–1940.
- [59] E. Morgado Jr., M.A.S. de Abreu, G.T. Moure, B.A. Marinkovic, P.M. Jardim, A.S. Araujo, *Chemistry of Materials* 19 (2007) 665–676.
- [60] K. Das, S.K. Panda, S. Chaudhuri, *Journal of Crystal Growth* 310 (2008) 3792–3799.
- [61] B. Wang, Y. Shi, D. Xue, *Journal of Solid State Chemistry* 180 (2007) 1028–1037.
- [62] N. Harsha, K.R. Ranya, K.B. Babitha, S. Shukla, S. Biju, M.L.P. Reddy, K.G.K. Warriner, *Journal of Nanoscience and Nanotechnology* 11 (2011) 1175–1187.
- [63] F. Cesano, S. Bertarione, M.J. Uddin, G. Agostini, D. Scarano, A. Zecchina, *Journal of Physical Chemistry C* 114 (2010) 169–178.
- [64] R. Menzel, A.M. Peiró, J.R. Durrant, M.S.P. Shaffer, *Chemistry of Materials* 18 (2006) 6059–6068.
- [65] C.C. Tsai, H. Teng, *Chemistry of Materials* 16 (2004) 4352–4358.
- [66] F. Maxim, P. Ferreira, P.M. Vilarinho, *Journal of Porous Materials* 18 (2011) 37–45.
- [67] J. Huang, Y. Cao, M. Wang, C. Huang, Z. Deng, H. Tong, Z. Liu, *Journal of Physical Chemistry C* 114 (2010) 14748–14754.
- [68] M. Sugita, M. Tsuji, M. Abo, *Bulletin of the Chemical Society of Japan* 63 (1990) 1978–1984.
- [69] S.T. Myung, N. Takahashi, S. Komaba, C.S. Yoon, Y.K. Sun, K. Amine, H. Yashiro, *Advanced Functional Materials* 21 (2011) 3231–3241.
- [70] S. Zhang, W. Li, Z. Jin, J. Yang, J. Zhang, Z. Du, Z. Zhang, *Journal of Solid State Chemistry* 177 (2004) 1365–1371.
- [71] M. Qamar, C.R. Yoon, H.J. Oh, D.H. Kim, J.H. Jho, K.S. Lee, W.J. Lee, H.G. Lee, S.J. Kim, *Nanotechnology* 17 (2006) 5922–5929.
- [72] X. Sun, Y. Li, *Chemistry – A European Journal* 9 (2003) 2229–2238.
- [73] L.Q. Weng, S.H. Song, S. Hodgson, A. Baker, J. Yu, *Journal of the European Ceramic Society* 26 (2006) 1405–1409.
- [74] G. Xiang, T. Li, J. Zhuang, X. Wang, *Chemical Communications* 46 (2010) 6801–6803.
- [75] A.A. Gribb, J.F. Banfield, *American Mineralogist* 82 (1997) 717–728.
- [76] M. Bouslama, M.C. Amamra, Z. Jia, M. Ben Amar, K. Chhor, O. Brinza, M. Abderrabba, J.L. Vignes, A. Kanaev, *ACS Catalysis* 2 (2012) 18884–21892.
- [77] M. Bouslama, M.C. Amamra, O. Brinza, S. Tieng, K. Chhor, M. Abderrabba, J.L. Vignes, A. Kanaev, *Applied Catalysis A: General* 402 (2012) 156–161.
- [78] S.-J. Kim, Y.-U. Yun, H.-J. Oh, S.H. Hong, C.A. Roberts, K. Routray, I.E. Wachs, *The Journal of Physical Chemistry Letters* 1 (2010) 130–135.
- [79] T. Gao, H. Fjellvåg, P. Norby, *Inorganic Chemistry* 48 (2009) 1423–1432.
- [80] A. Gajović, I. Friščić, M. Plodinec, D. Iveković, *Journal of Molecular Structure* 924–926 (2009) 183–191.
- [81] L. Qian, Z.L. Du, S.Y. Yang, Z.S. Jin, *Journal of Molecular Structure* 749 (2005) 103–107.
- [82] D.V. Bavykin, J.M. Friedrich, A.A. Lapkin, F.C. Walsh, *Chemistry of Materials* 18 (2006) 1124–1129.
- [83] Y.V. Kolen'ko, K.A. Kovnir, A.I. Gavrilov, A.V. Garshev, J. Frantti, O.I. Lebedev, B.R. Churagulov, O.G.V. Tendeloo, M. Yoshimura, *Journal of Physical Chemistry B* 110 (2006) 4030–4038.
- [84] A. Riss, T. Berger, H. Grothe, J. Bernardi, O. Diwald, E. Knozinger, *Nano Letters* 7 (2007) 433–438.
- [85] E. Horvath, A. Kukovecz, Z. Konya, I. Kiricsi, *Chemistry of Materials* 19 (2007) 927–931.
- [86] W. Su, J. Zhang, Z. Feng, T. Chen, P. Ying, C. Li, *Journal of Physical Chemistry C* 112 (2008) 7710–7716.
- [87] T. Ohsaka, F. Izumi, Y. Fujiki, *Journal of Raman Spectroscopy* 7 (1978) 321–324.
- [88] T. Beuvier, M. Richard-Plouet, L. Brohan, *Journal of Physical Chemistry C* 113 (2009) 13703–13706.
- [89] M. Ben Yahia, F. Lemoigno, T. Beuvier, J.S. Filhol, M. Richard-Plouet, L. Brohan, M.L. Doublet, *Journal of Chemical Physics* 130 (2009) 204501.
- [90] W. Wang, J. Zhang, H. Huang, Z. Wu, Z. Zhang, *Colloids and Surfaces A* 317 (2008) 270–276.
- [91] J. Yu, H. Yu, *Materials Chemistry and Physics* 100 (2006) 507–512.
- [92] Y. Paz, Z. Luo, L. Rabenberg, A. Heller, *Journal of Materials Research* 10 (1995) 2842–2848.
- [93] J. Yu, X. Zhao, *Materials Research Bulletin* 35 (2000) 1293–1301.
- [94] C. Guillard, B. Beaugiraud, C. Dutriez, J.M. Herrmann, H. Jaffrezic-Renault, M. Lacroix, *Applied Catalysis B* 39 (2002) 331–342.